# Fabrication of Extremely Smooth Blazed Diffraction Gratings

by

## Chih-Hao Chang

B.S., Mechanical Engineering, Georgia Institute of Technology (2002)
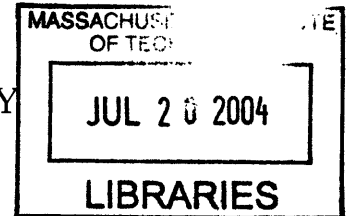
Submitted to the Department of Mechanical Engineering
in partial fulfillment of the requirements for the degree of

Master of Science in Mechanical Engineering

at the

MASSACHUSETTS INSTITUTE OF TECHNOLOGY

June 2004

Author . . . . . . . . . . . . . . . . . . . . . . . . . . . . . . . . . . . . . . . . . . . . . . . . . . . .
Department of Mechanical Engineering
May 7, 2004

Certified by . . . . . .
Mark L Schattenburg
Principal Research Scientist
Thesis Supervisor

Certified by . . . . . . . . . . . . . . . . . . . . . . . . . .
George Barbastathis
Edgerton Assistant Professor, Mechanical Engineering
Thesis Supervisor

Accepted by . . . . . . . . . . . . . . . . . . . .
Ain A. Sonin
Chairman, Department Committee on Graduate Students

# Fabrication of Extremely Smooth Blazed Diffraction Gratings

by

Chih-Hao Chang

## Abstract

High efficiency diffraction gratings are important in a variety of applications, such as optical telecommunications, lithography, and spectroscopy. Special interest has been placed on blazed diffraction gratings for their ability to enhance diffraction intensity at the specular reflection angle off the blazed facets. In this thesis I will report a novel process for fabricating extremely smooth blazed diffraction gratings with 200 nm-period. The blazed grating is fabricated using interference lithography and anisotropic etching, then replicated using nanoimprint lithography. This process was developed for fabricating the off-plane blazed diffraction gratings for the NASA *Constellation-X* x-ray space telescope.

In order for x-rays to reflect effectively through grazing incidence reflection, the gratings will be coated with high atomic number materials, such as gold. Deposition of thin metal film often develops residual stress that adds out-of-plane distortion. In this thesis the out-of-plane distortions due to thin metal films are analyzed using wavefront aberration functions known as the Zernike polynomials. The thin film stress is proved to be linearly related to the change of the $Z_{21}$ Zernike coefficient. The anisotropic material properties of silicon are taken into account in the derivation, and a prediction of lattice dependent distortion is proposed.

Thesis Supervisor: Mark L Schattenburg
Title: Principal Research Scientist

Thesis Supervisor: George Barbastathis
Title: Edgerton Assistant Professor, Mechanical Engineering

# Acknowledgments

First of all I would like to thank my research advisor Dr Mark Schattenburg. The guidance and support he provided were invaluable to me. I owe the first 2 years of my graduate education to him. I thank Dr Ralf Heilmann for the knowledge he shared as well, especially topics involving x-rays. I thank Bob Fleming and Eddie Murphy for passing on their expertise and experiences to me on all those sleepless mornings. If it were not for them i probably blew up the *Space Nanotechnology Lab* on numerous occasions. I thank Jimmy Carter and Jim Daley from the *NanoStructures Lab* for their technical help and advice. I also thank all the staff at MTL.

I need to thank my officemate, Mireille, the glass queen, for being a great friend. Those endless discussions on our research, future goals, and life have been truly amazing. I thank my labmates: Chulmin, you can't never eat as much noodle as Carl. Juan, the marathon runner, thanks for getting the NanoRuler to work even when things just break. Carl, the double noodle double meat funny guy, you need to come back and visit so we can all get ramen again. Paul, thanks for answering those geophone emails when you are in Hawaii. Yanxia, thanks for teaching me the RCA clean. Craig, I really dislike the SH, but GO YELLOWJACKETS! Andy, your SH software is amazing: When things look funny, "andy" it. I also need to thank Euclid for all the help with the AFM.

I thank all my friends here at MIT, especially Lisa the "PGD", Chen the "HSM", and Tim the "HPT". Rocsa people you guys are great! Life here would of been rather quiet without you all.

Most importantly I thank my family. I thank my wonderful parents, they gave me everything. I thank my big beautiful sister, for all her support and encouragement. She showed me the way. I thank my little cute sister, for her funny stories and request that make me laugh.

# Contents

9

# List of Figures

14

# List of Tables

# Chapter 1

# Introduction

*"It is difficult to point to another single device that has brought more important experimental information to every field of science than the diffraction grating."*

*-G. R. Harrison* [29].

The diffraction grating is a fundamental optical element that is used in almost every aspect of experimental science. It has vital roles in spectroscopy, lithography, optical telecommunications, and many other applications. A special class of diffraction gratings is the blazed grating. These gratings have a saw-tooth profile instead of the conventional rectangular profile. Special interest has been placed on the blazed grating for their ability to maximize diffraction efficiency at the specular reflection angle off the blazed facets. [24] is a good reference for diffraction gratings, and it also describes a brief history. In this thesis I will present the fabrication process of extremely smooth blazed diffraction gratings with sub-micrometer spatial period. The process was developed to fabricate x-ray diffraction gratings for NASA's next generation x-ray space telescope *Constellation-X*.

## 1.1   Diffraction Gratings

Diffraction is an optical phenomenon caused by the interference of scattered light from periodic structures. There are two common types of diffraction gratings. The first

17
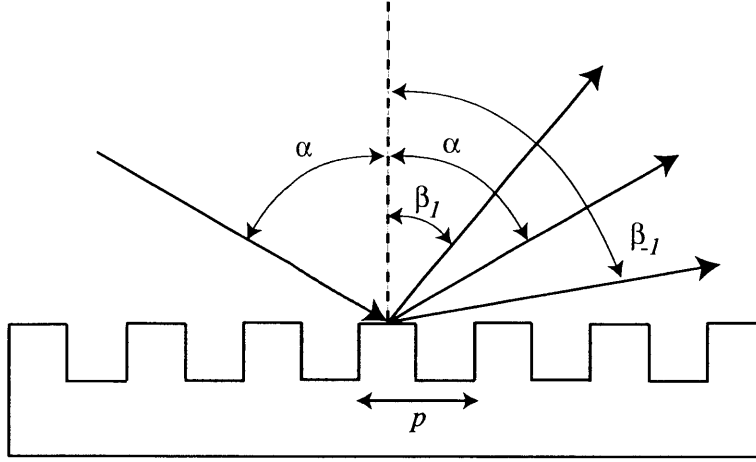
Figure 1-1: The directions of diffracted orders for an in-plane reflective diffraction grating.

are the transmission gratings, in which the diffracted orders are transmitted through the grating. The second are the reflective gratings, in which the diffracted orders are reflected. In some cases, when the material of the grating is not fully opaque or transparent, the grating will have both reflected and transmitted orders. The process outlined in this thesis is designed for reflective gratings.

The directions of the diffracted orders off a reflective diffraction grating, shown in Figure 1-1, can be described by the general grating equation,

$$\frac{n\lambda}{p} = \sin\alpha + \sin\beta, \tag{1.1}$$

where $n$ is the diffracted order, $\lambda$ is the wavelength of light being diffracted, $p$ is the spatial period of the grating, $\alpha$ is the incident angle, and $\beta$ is the diffracted angle. Both $\alpha$ and $\beta$ are measured from the grating normal direction.

From Equation 1.1 the physical limitations of a diffraction grating can be observed. In one extreme, when $\lambda/p$ approaches 2, the diffracted orders spread further and further apart, until they can no longer be observed. In the other extreme, when $\lambda/p$ approaches 0, the diffracted orders will be so close to one another that they can not be analyzed separately. The resolving power, $R$, of a grating is defined as,
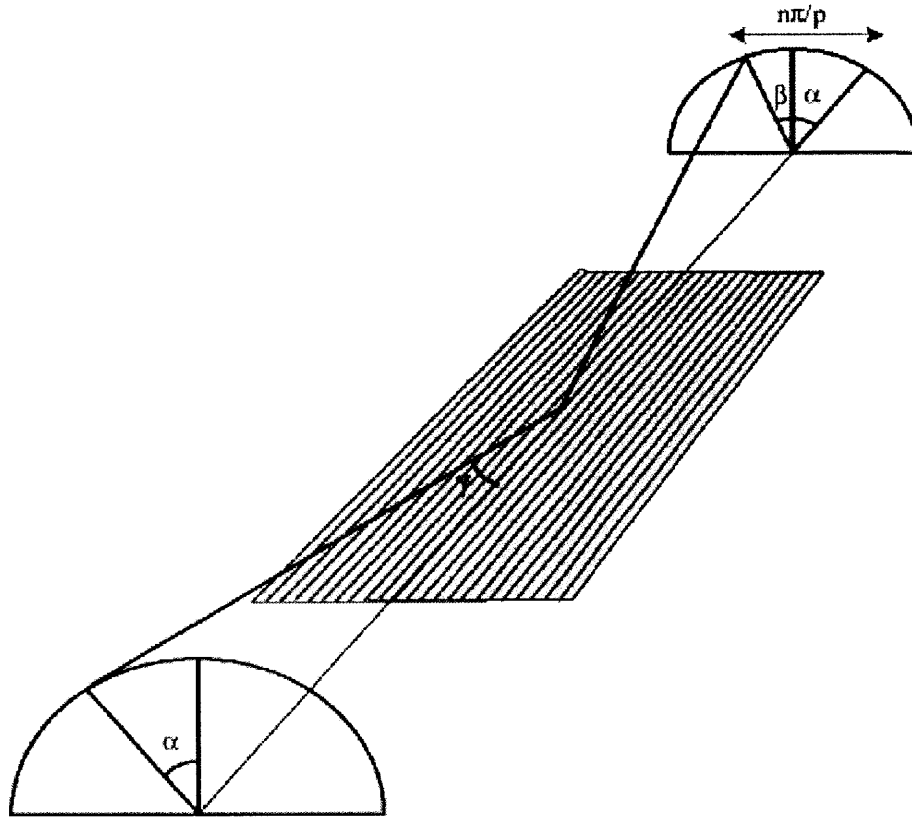
Figure 1-2: The directions of diffracted orders for an off-plane diffraction grating.

$$R = n\frac{D}{p},$$ (1.2)

where $n$ is the diffraction order, $D$ is the size of the illumination, and $p$ is the grating period. Therefore the reduction of spatial period increases the grating's resolving power, which is essential when doing spectroscopy on higher energy sources.

There are two different mount geometries that can be used for a reflection grating. The in-plane mount, shown in Figure 1-1, has the incident plane parallel with the grating lines. The off-plane mount, shown in Figure 1-2, has the incident plane perpendicular with the grating lines. The diffracted orders for an off-plane mount will lie in a half cone, also shown in Figure 1-2.

19
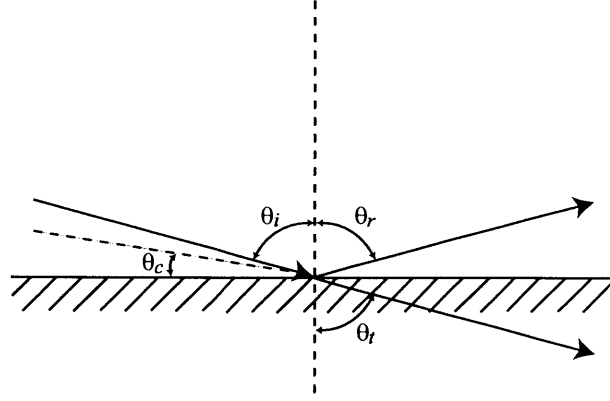
Figure 1-3: A electromagnetic wave interacting with an interface of two mediums.

## 1.2   Grazing Incidence Reflection

Due to its high photon energies, x-rays are incredibly hard to manipulate. Most materials, at the x-ray spectrum, are transparent. The low optical index contrast between materials and vacuum makes refractive optics ineffective. Reflectivity from normal incidence illumination is also low for the same reason. A method to overcome this challenge is by grazing incidence reflection, when the x-rays are reflected by total external reflection [22]. The physics of this reflection can be analyzed through the Fresnel Equation, which describes the interaction of an electromagnetic wave at an interface of two mediums, as shown in Figure 1-3. The Fresnel Equation is given by,

$$R_\perp = \frac{n_i \ \cos\theta_i \ - n_m \ \cos\theta_t}{n_i \ \cos\theta_i \ + n_m \ \cos\theta_t}, \tag{1.3}$$

for TE polarization, and

$$R_| = \frac{n_m \ \cos\theta_i \ - n_i \ \cos\theta_t}{n_m \ \cos\theta_i \ + n_i \ \cos\theta_t}, \tag{1.4}$$

for TM polarization light. Here $R$ is the reflectivity, $n_i$ and $n_i$ are the ambient and material optical index, and $\theta_i$ and $\theta_t$ are the incident and reflected angles, respectively.

For high-energy x-rays, the optic index is complex, given by,

$$n = 1 - \delta - i\beta, \tag{1.5}$$

20

where $\delta$ and $\beta$ are related to the optical refractive and absorption index, respectively. Assuming ambient of vacuum, and the material is not absorbing[1], Equations 1.3 and 1.4 yield,

$$R_\perp = \frac{(1 - \delta_i) \cos \theta_i \ - (1 - \delta_m) \cos \theta_t}{(1 - \delta_i) \cos \theta_i \ + (1 - \delta_m) \cos \theta_t}, \tag{1.6}$$

and,

$$R_| = \frac{(1 - \delta_m) \cos \theta_i \ - (1 - \delta_i) \cos \theta_t}{(1 - \delta_m) \cos \theta_i \ + (1 - \delta_i) \cos \theta_t}. \tag{1.7}$$

Substituting $\theta_i$ for $\theta_t$ by using Snell's law,

$$R_\perp = \frac{(1 - \delta_i) \cos \theta_i \ - (1 - \delta_m)\sqrt{1 - [(\frac{1-\delta_i}{1-\delta_m}) \sin \theta_i]^2}}{(1 - \delta_i) \cos \theta_i \ + (1 - \delta_m)\sqrt{1 - [(\frac{1-\delta_i}{1-\delta_m}) \sin \theta_i]^2}}. \tag{1.8}$$

and,

$$R_| = \frac{(1 - \delta_m) \cos \theta_i \ - (1 - \delta_i)\sqrt{1 - [(\frac{1-\delta_i}{1-\delta_m}) \sin \theta_i]^2}}{(1 - \delta_m) \cos \theta_i \ + (1 - \delta_i)\sqrt{1 - [(\frac{1-\delta_i}{1-\delta_m}) \sin \theta_i]^2}}, \tag{1.9}$$

For angle $\theta_c$ such that,

$$\sin \theta_i < \frac{1 - \delta_m}{1 - \delta_i} = \cos \theta_c \tag{1.10}$$

equation 1.8 and 1.9 can be simplified to yield reflectivities of 1. $\theta_c$ is defined as the critical angle, when the incident light is 100% reflected by total external reflection. This phenomenon is known as grazing incidence reflection, and it is the physics behind grazing incident reflection gratings. In reality x-rays are absorbed in any medium, and the reflectivity will be reduced.

## 1.3   Space Telescopes and *Constellation-X*

Exploration of our universe has long been an interest for astrophysicists. Telescopes and observatories are the primary instrumentations for this purpose. In addition

---

[1]$\beta$ is usually in the order of $10^{-2}$ to $10^{-6}$.
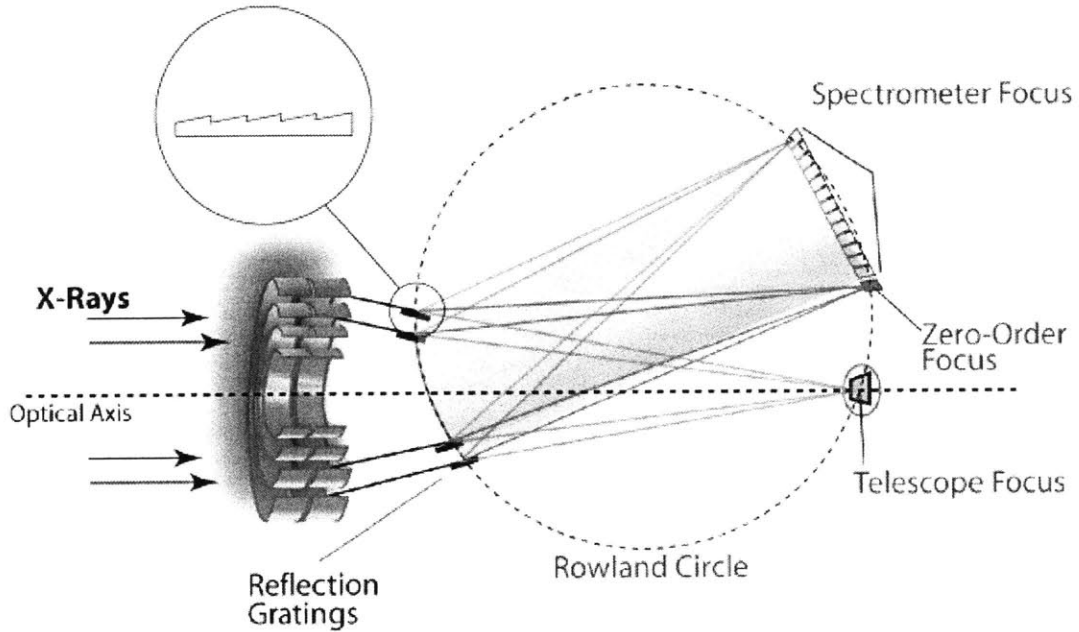
Figure 1-4: Configuration of a x-ray space telescope.

to visual images, spectroscopy of the photon energies can determine information on material composition. For celestial sources with high energies, such as those in the x-ray or deep-UV spectrum, ground based telescopes are impractical because most of those radiations are absorbed by the atmosphere. Thus space telescopes in orbit were purposed. Mongrard [23] gives a detailed history of space telescopes. A typical optical configuration for a x-ray space telescope is shown in Figure 1-4.

The two gold rings are paraboloids followed by hyperboloids, set up in a Wolter configuration. The x-rays will reflect by grazing incidence whenever the local slope is less than the critical angle. The focus of the paraboloid coincides with one of the foci of the hyperboloids, so that the focus of the compound system is at the other focus of the hyperboloids. The diffraction gratings are positioned on a Rowland circle. In this diagram the gratings are in an in-plane mount, so the diffracted orders will lie on the same axis, shown in Figure 1-4.

*Constellation-X* is NASA's next generation space telescope for the x-ray spectrum. The primary purpose of the process, described in this thesis, is for the off-plane grazing-incident reflection grating to be used for *Constellation-X*. The required

grating area for this space mission will be in the order of 100 square meters. Thus, other than the grating performance, the time and cost factors are also important.

## 1.4  Outline of Thesis

Chapter 2 will describe the technique of anisotropic etching and alignment issues. Chapter 3 will outline the fabrication process of the blazed grating in silicon. Chapter 4 will introduce the implementation of a replication process for the blazed gratings. Chapter 5 will discuss thin metal film distortions by using the Zernike polynomials. Chapter 6 will present the comparison x-ray diffraction efficiency results.

# Chapter 2

# Anisotropic Etching

## 2.1 Introduction

The anisotropic etching properties of silicon crystals lead to processes that can fabricate unique, remarkable structures in the micro-nano scale. The enormous difference in etch rates between the different crystal lattice directions create surfaces that are, theoretically, atomically smooth. Integrating such etching technique into the fabrication of x-ray diffraction gratings promises straight profiles and extremely smooth surfaces. This process also finds many applications in MEMS, integrated optics, and numerous other disciplines.

An important factor in anisotropic etching is the alignment of the masks to the desired crystal lattice direction. Any error will undercut the mask and result in undesired atomic steps on the etched surfaces. This chapter will describe the basic principles of anisotropic etching, present examples of anisotropically etched structures, and highlight the alignment issues.

## 2.2 Single Crystal Silicon

The silicon wafers used in microfabrication processes are grown from a single silicon crystal seed, and therefore the silicon atoms are arranged in a crystal lattice. Silicon's crystalline structure is the fundamental reason for anisotropic properties. The atomic
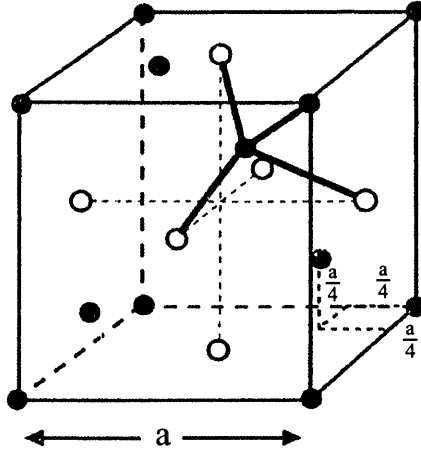
Figure 2-1: Atomic structure of silicon crystal.

lattice of silicon is a diamond-type structure that can be visualized by two off-set face-centered cubic cells, shown in Figure 2-1. The lattice parameter $a$ for silicon is 0.544 nm.

To distinguish between different directions and planes in a crystal lattice, the Miller indices are used[1]. Silicon has three different basic family plane orientations, the {100}, the {110}, and the {111} planes. The {111} planes have the highest atomic packing density, while {100} planes have the lowest.

When etched with a properly selected mask in alkaline based solutions such as KOH, NaOH, or Tetramethyl ammonium hydroxide (TMAH), the etch rate for the ⟨111⟩ directions is found experimentally to be two orders of magnitude lower than for the ⟨110⟩ and ⟨100⟩ directions. The etch rate ratios of some commonly used anisotropic etchant are listed in Table 2.1. Since the etch rates for the ⟨111⟩ directions are so small, the planes normal to these directions, the {111} planes, are virtually unetched. As the result, the profile of the etched structures will consists of only the {111} planes, and these planes will be extremely smooth.

One drawback of anisotropic etchant is the low etch rate. For even the fastest direction ($\sim$1 $\mu$m/min), it is relatively slow compared to isotropic etchants (up to 50

---

[1]The Miller indices is a widely used vector notation that can easily define a crystal's basic geometric properties such as plane, direction, and angle. For further reading refer to [19].

26

| Etchant | Etch Ratio (100)/(111) | Etch Masks (Etch Rates) |
|---|---|---|
| KOH | ~400 | $SiO_2$ (~2.8 nm/min); $Si_3N_4$ (not etched) |
| Ethylene-diamine pyro-catechol (EDP) | ~35 | $SiO_2$ (0.2-0.5 nm/min); $Si_3N_4$ (~0.1 nm/min) |
| Tetremethyl ammonium hydroxide (TMAH) | 12.5 - 50 | $SiO_2$ (~0.1 nm/min) |

Table 2.1: Anisotropic etch rates for some commonly used etchant, as reported in [19]

$\mu$m/min). In addition, the surfaces other than the {111} planes will be rough over a wide band of spatial frequencies. Both of these factors are mitigated with the increase of temperature during etching. Thus most anisotropic etching is done at 80-85$^\circ$C. For applications where the desired profiles consists of only (111) planes these drawbacks can be overlooked.

## 2.3  Chemistry of Anisotropic Etching

While there is not a mutually agreed model, there are many proposed theories to describe the kinetics behind the anisotropic etching properties of silicon. When examining the atomic structures of the three crystal planes, the bond densities are 1:0.71:0.58 for the {100}:{110}:{111} surfaces. Since there is a direct correlation between available bond density and etch rate, the etch rate of {100} planes is predicted to be higher than {111} planes. Even though the difference in bond densities is a logical argument, the etch rate difference of two magnitude orders is surprising. Kendall [17] proposed that the {111} planes oxidizes at a faster rate than the other crystal planes due to the close proximity of the neighboring atoms. The oxide then serves as a protection to the {111} planes during etching.

Another theory by Seidel *et al.* [27] states that the difference in etch rates is due

to the differences in backbone geometries and activation energies. The {111} planes have three back bonds (out of four total covalent bonds) below the surface, therefore these bonds are shielded from chemical reaction. Also, Elwenspoek [9] proposed that anisotropic etching is dependent on the degree of atomic smoothness of different crystal planes {100}, {110}, and {111}. The kinetics of forming smooth surfaces were studied, and Elwenspoek concluded that smooth surfaces such as the {111} planes have a nucleation barrier which protects itself. Such barriers are not present in rougher surfaces such as the {100} and {110} planes, contributing to higher etch rates on these directions.

## 2.4   Anisotropically Etched Structures

One of the simplest and most common structure to fabricate with anisotropic etching is the inverted triangular trenches. These structures are fabricated using (100) silicon wafers, with the mask aligned along the [110] direction. As an example of such structures, 200 nm-period gratings with inverted triangular profiles was fabricated. The etchant used was KOH (20% by weight, at room temperature), selected because it has the highest etch rate ratio.

The grating lines were patterned 200 nm-period with 50% duty cycle using an interference lithography setup in the Space Nanotechnology Lab at MIT [10]. The setup operates on a Ar ion laser at $\lambda = 351.1$ nm, and the beams are at half angle of $\sim 61.4^o$. The IL setup is depicted in Figure 2-2.

The process utilizes a bilevel resist scheme, with 200 nm of Sumitomo PFI-34a2 positive resist on top of 49 nm of Brewer Science i-Con-7 Anti-Reflection Coating (ARC). Under the resist layer stack there is 30 nm of silicon nitride for KOH etch mask. The fabrication process diagram is illustrated in Figure 2-3.

After the pattern is transfered to the hardmask, the sample is etched in a KOH bath for 5 minutes. The nitride mask was removed in HF. The resulting profile, taken by a scanning electron microscope (SEM), is shown on Figure 2-4. The top surface of the grating was protected by nitride and was not etched. The side walls represent
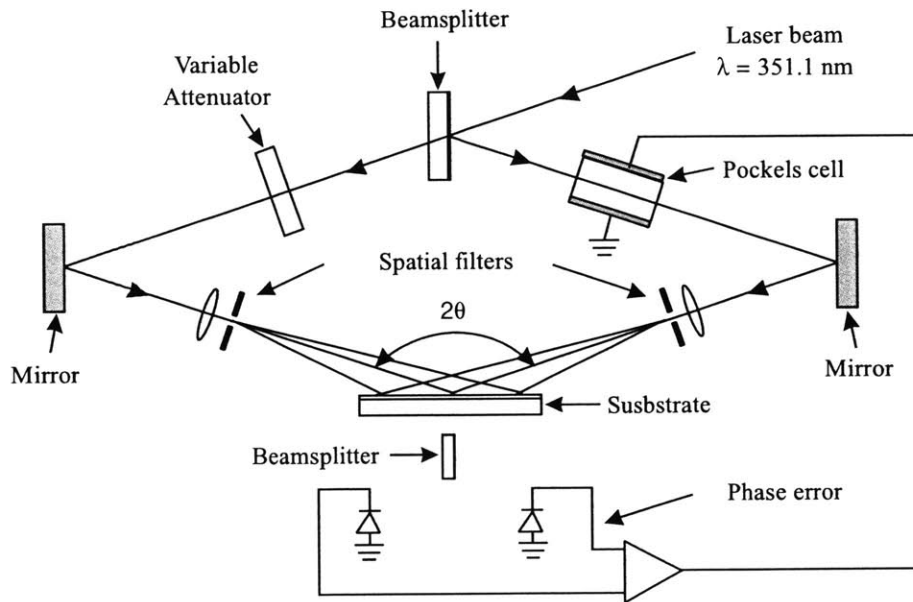
Figure 2-2: Interference lithography setup at MIT's Space Nanotechnology Lab.
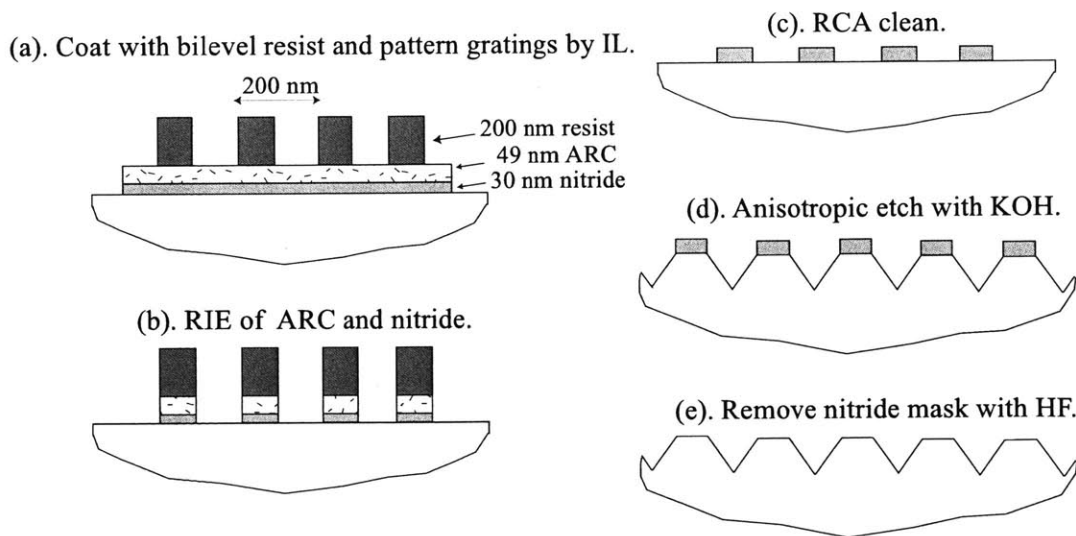


Figure 2-3: Process diagram for 200 nm-period gratings with inverted triangular profile.
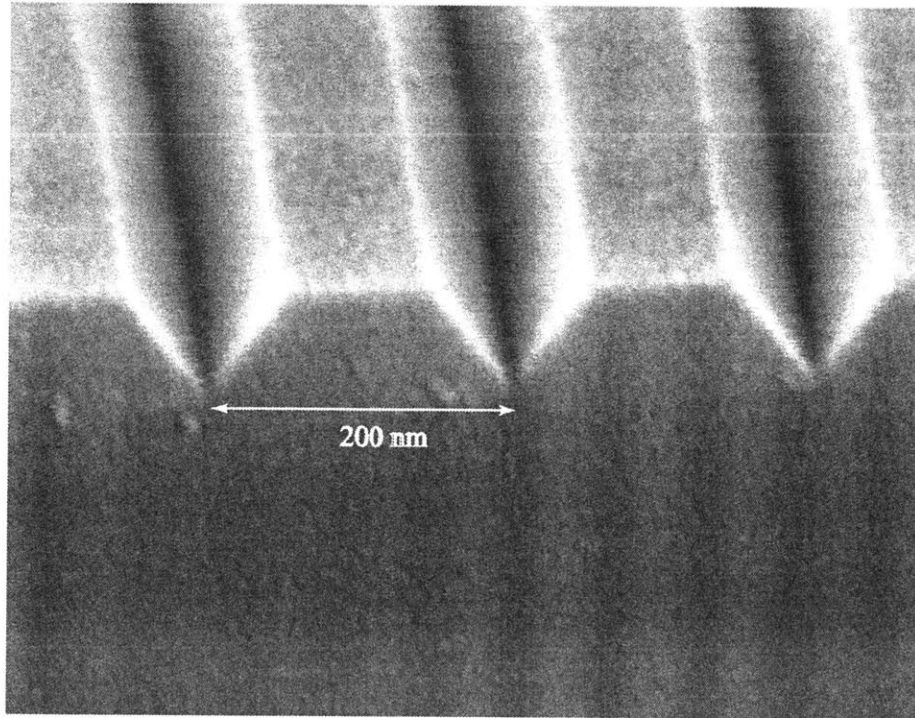
Figure 2-4: SEM of 200 nm-period grating with inverted triangular profile.

the (111) planes and is sloped at $\sim 54.7^o$ from the wafer normal.

## 2.5 Alignment

Careful alignment of the mask to the desired crystal direction is critical during anisotropic etching. Misalignments result in undercutting of the etch mask on the macroscale, and atomic lattice steps in the (111) planes on the microscale. Figure 2-5 illustrates both of these effects. Theoretically, atomically smooth surfaces can be obtained if the alignment is perfect. The degree of surface roughness worsens with increasing misalignment. The wafer flats provided by commercial vendors only give an approximation of the crystal lattice directions, and have errors in the range of $\pm 0.5^o$. The angular error also varies between wafers that are not from the same batch. Alignment of the mask to the provided wafer flat is not accurate enough if extremely smooth surfaces are desired. Therefore a process to determine the crystal lattice direction is extremely important. The etch mask will then be aligned to the
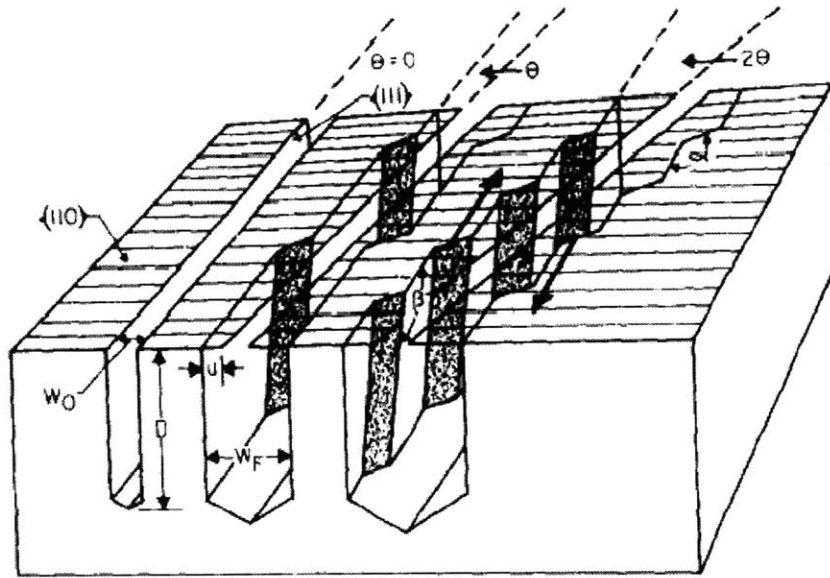
Figure 2-5: The macroscale and microscale effects of misalignment during anisotropic etching, from [16]

determined crystal lattice, instead of the provided wafer flats.

Another challenge involved is the alignment of the etching mask to the determined crystal lattice direction. In an IL setup it is difficult to align the two interfering beams so that the interference fringes will be perfectly vertical. In this section the translational error of the two interfering arms will be related to the rotational error of the fringes. Also, a moiré technique to experimentally determine the interference fringe rotation will be described in this section.

### 2.5.1 Determining Crystal Lattice Direction

One method by Ciarlo [8] proposed using a pre-etch alignment pattern to determine the correct lattice direction. A set of 3 mm long and 8 $\mu$m lines, each with a offset 0.1$^o$, were patterned at the corner of the silicon wafer. The line pattern was then etched in the same anisotropic etchant that will be used. Upon examination, the line structure with the least undercutting and surface roughness will represent the true

crystal lattice direction. Even though this process is time consuming and troublesome, it has been reported to achieve alignment accuracy better than $0.05^o$.

Another method in determining the true crystal lattice direction of a silicon wafer is based on cleaving. Silicon, due to it's crystal structure, cleaves more favorably along the [110] directions. For example, a (100) silicon wafer with a primary flat in the [110] direction will cleave more easily parallel and perpendicular to the flat. A (111) silicon wafer cleaves in three directions at $60^o$ to one another. Therefore, by cleaving a wafer sample, the true orientation of the [110] directions can be found, and the offset can be measured using a caliper. The angular off-set of the [110] direction to the wafer flat can then be corrected. This method is destructive, but only one wafer needs to be cleaved per batch, assuming that the wafer flat angular offset is the same within a batch. The accuracy of this process is dependent on the accuracy of the caliper, and is approximated at $\sim 0.017^o$. This method was used for all the samples fabricated.

## 2.5.2 Alignment of Interference Fringes

Interference lithography interferes two mutually coherent beams to form a sinusoidal intensity function[2] to pattern periodic structures. The period of the image grating is given by

$$\Lambda = \frac{\lambda}{2 \sin \theta},$$ 
(2.1)

where $\Lambda$ is the period, $\lambda$ is the wavelength of light used, and $\theta$ is the half angle between the beams. During the exposure it is important that the image grating is aligned properly to the desired lattice direction on the wafer. The orientation of the image grating is dependent on the location of the two light sources. As implied in Figure 2-6, any translational errors, *2d*, in $z$ between the two sources will lead to a rotational error in the image grating. Taking account of this translational error, the angular dependence of the image grating can be found by calculating the interference

---

[2]The interference fringes will be referred to as the image gratings

between the two waves. To simplify calculations, two plane waves will be used. The plane waves are misaligned by $2d$ in the $z$-direction, and can be described as

$$E_1(x, y, z, t) = A_1 e^{(jk(ya\sin\theta - xa\cos\theta + zd - \omega t))}, \qquad (2.2)$$

and,

$$E_2(x, y, z, t) = A_2 e^{(jk(-ya\sin\theta - xa\cos\theta - zd - \omega t))}, \qquad (2.3)$$

where $A_1$ and $A_2$ are the amplitude, $a$ is the beam length, and $k = 2\pi/\lambda$ is the propagation number. Adding up the intensities and simplifying obtains,

$$|E_1 + E_2|^2 = (A_1^2 + A_2^2)[1 + \frac{2A_1 A_2}{A_1^2 + A_2^2} \cos(k[2ya\sin\theta + 2zd])]. \qquad (2.4)$$

The $\cos\phi$ term represents the fringe pattern, and the following equation can be derived

$$\frac{\lambda}{2} = ya\sin\theta + zd, \qquad (2.5)$$

Equation 2.5 states that due to the $z$-offset, the image grating is a function of both $y$ and $z$. An offset of $2d$ will result in a rotation of $\tan^{-1}(d/\sin\theta)$ from vertical. To get an idea of the magnitude of errors, for $a = 1$ m, and fringe offset of $0.02^o$, $d \approx 610$ $\mu$m.

For accurate alignment, instead of trying to adjust the two arms, along with all the optics, another approach is more feasible. The angular error of the image grating can be characterized and then compensated by adjusting the wafer with an angle offset. Since the pattern being exposed is beyond the resolution of optical microscopes, electron microscopes need to be used. The process of determining the angular offset of sub-nm grating lines is extremely tedious and time consuming. A simple process involving moiré pattern is used to solve this problem.

33
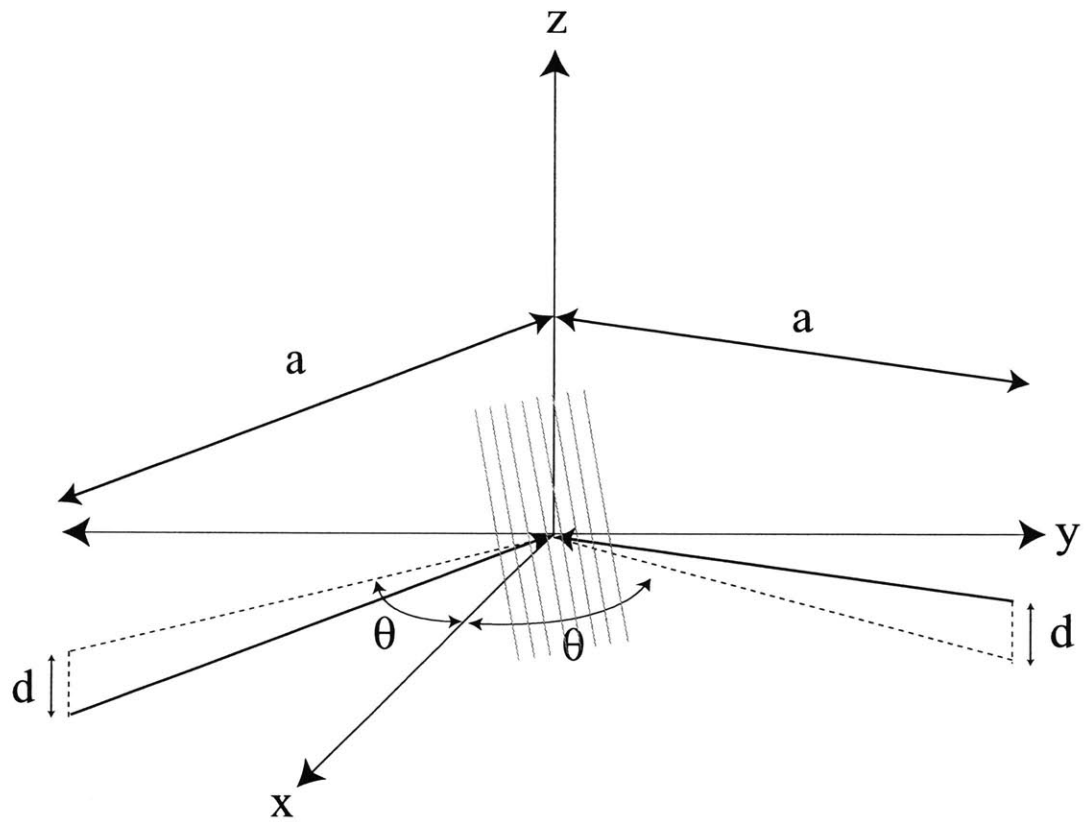
Figure 2-6: Image grating's angular dependence on $z$-translational errors between the two sources.
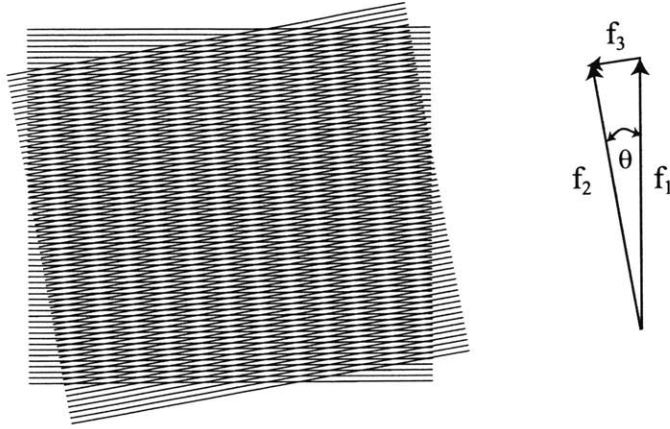
Figure 2-7: Moiré pattern of two sets of grating lines with an angle offset and their frequency vectors.

### 2.5.3 Characterization of Fringe Rotation using Moiré Patterns

In order to determine the image grating's angular offset from vertical, a technique involving moiré pattern is used. A moiré pattern is formed between two images when their spatial periodicity are relatively close. It can also be described as a beat frequency vector between the spatial frequencies of two images. Figure 2-7 demonstrates the concept of moiré pattern with two identical set of 64 lines with a $10^o$ offset to each other. Assume that the spatial frequencies of the two sets of lines are same and equal to $f$. Using simple vector manipulation the spatial frequency of the moiré pattern can be found,

$$f_3 = 2f \sin \frac{\theta}{2}. \tag{2.6}$$

Where $\theta$ is the angle offset. For $f_1 = f_2 = 64$ lines/length and $\theta = 10^o$, as depicted in Figure 2-7, $f_3 \approx 11.2$ lines/length. The moiré pattern effect magnifies the periodicity of two gratings with an angular offset in a way that can be calculated. The spatial period magnifying factor can be calculated to be,

35

$$M = \frac{f}{f_3} = (2\sin(\frac{\theta}{2}))^{-1} \approx \frac{1}{\theta}, \tag{2.7}$$

for small $\theta$. Using the moiré pattern technique, the 200 nm-period grating can be magnified so that the angular offset can be characterized. The wafer will be exposed twice, at offsets of $\pm 0.5^o$ to a reference angle. This offset angle correspond to a magnification of 57.3 on the moiré pattern. After the exposures the two sets of 200 nm-period grating lines will have a moiré grating pattern that has period of $\sim 11.5$ $\mu$m. The angle offset of the wafer flat to the reference angle can then be easily characterized using an optical microscope.

## 2.6 Conclusion

Anisotropic etching of silicon is a process that is capable of fabricating extremely smooth surfaces. In order to fabricate structures with minimal atomic steps and undercutting, alignment of the etch mask to the crystal lattice is critical. By using a pre-etch alignment pattern or the cleaving technique, the crystal lattice can be determined more accurately than the provided wafer flats. In addition, the exact orientation of the interference-produced image grating can be characterized using the moiré pattern. These alignment techniques will reduce the surface roughness of the anisotropically etched structures considerably.

# Chapter 3

# Fabrication of Blazed Diffraction Gratings

## 3.1    Introduction

There are many methods in which these blazed diffraction gratings can be fabricated. Those include mechanical ruling, lithography patterning and plasma etching, and anisotropic etching. These methods are explained with further detailed in [13]. In fabricating diffraction gratings, one of the most important factors is the roughness of the blazed facets. Undesired scattering is found to be proportional to the square of the surface roughness [3]. Anisotropically etched blazed gratings have very low roughness, and have demonstrated excellent results at the $\mu$m period [12]. In this chapter the fabrication of anisotropically etched 200 nm-period grating with $7^o$ blaze angle will be described. This type of grating is designed for the NASA space x-ray telescope *Constellation-X.*

## 3.2    Silicon Orientation Selection

The selection of the orientation of the silicon wafer to use is important in fabricating blazed diffraction gratings, as the etched profile is entirely dependent on the crystal lattice. In Chapter 2 regular (100) wafers were used to fabricate inverted triangular
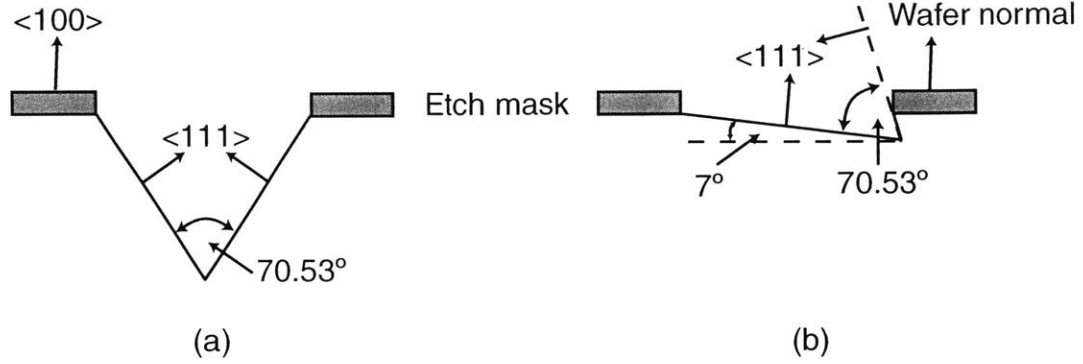
Figure 3-1: The cross-section profiles of anisotropically etched, (a) (100) wafer, and (b) wafer with lattice rotated ~50°.

structures. It is desired to use the etched surfaces as the blazed facets due to its smoothness. Furthermore, to increase diffraction efficiency, the area of the surface should be maximized, while minimizing the other surfaces. If the crystal lattice is rotated along the [110] direction, then the etched profile would be asymmetrical. Figure 3-1 illustrates this concept. Figure 3-1(a) shows the cross-section view of a (100) wafer anisotropically etched, and Figure 3-1(b) shows the etched profile if the lattice is rotated ~50° counter-clockwise around [110], which is pointing out of the page.

The wafer orientation that was chosen has the wafer normal rotated 7° from the [111] direction along the [1$\bar{1}$0] axis. The grating lines will then be aligned to the [1$\bar{1}$0] direction. These off-cut wafers naturally had to be specially ordered from Nova Electronics, and the off-cut angle has an error specification of ± 0.25°.

## 3.3  Layer Design

The design of the resist layers is important in interference lithography patterning. If not properly designed, the beam arms will reflect off the silicon interface and interfere with the opposing beam arm. This interference will produce undesired standing waves. A layer of anti-reflective coating (ARC), is thus needed to absorb the reflected light. This coating is usually spun on under the resist layer. Grating lines patterned

38

by interference lithography without an ARC layer will have wavy resist side walls.

ARC is typically designed to absorb a selected bandwidth of the light spectrum. For the laser used ($\lambda$=351.1 nm), Brewer Science ARC-i-con-7 has complex index $n = 1.6462 - j\, 0.3978$. The real index is close to the refractive index for resist, so there will be little reflection off the resist/ARC interface. Most of the light will then enter the ARC layer and be absorbed. The light reflected off the resist/ARC interface will not be absorbed by the ARC and will interfere with the other beam arm. This reflectivity is small ($\sim 2\%$) since the refractive index of the resist and ARC match well.

Ideally thicker ARC layer is better, since it will absorb the reflected light more. However, the developed resist is needed as an etch mask for the ARC during the oxygen reactive ion etching (RIE). The selectivity of oxygen RIE for resist and ARC is essentially one, since they are both polymer materials. Therefore the thickness of the ARC needs to be less than the resist thickness for better pattern transfer.

To optimize the thickness of the ARC layer, a simulation of reflectivity at the resist/ARC interface can be examined. The reflectivity simulation is based on a model used by Schattenburg *et al.* [26]. The layer configuration will be resist, ARC, and KOH etch mask silicon nitride on top of silicon. For a stack with 200 nm of resist, ARC, and 30 nm of silicon nitride on top of silicon, Figure 3-2 simulates the reflectivity at the resist/ARC interface as a function of ARC thickness.

A local minima can be seen around 49 nm, corresponding to a reflectivity of less than 0.5%. This thickness of ARC is also ideal for the oxygen RIE step, since it is about four times smaller than the resist thickness.

## 3.4 Fabrication Process

Details of the fabrication process for the 200 nm-period grating with $7^o$ blaze angle will be described in this section. The process includes interference lithography for patterning, RIE for pattern transfer, and KOH for wet anisotropic etching. The process flow diagram is shown in Figure 3-3. The process recipe is listed with more details in Appendix A.

| Material | $n_k$ | $\eta$ | Thickness |
|---|---|---|---|
| Air | 1 | 0 | inf |
| Sumi. PFI-34a resist | 1.7 | -0.01 | 200 nm |
| Brewer ARC-i-con-7 | 1.6462 | -0.3978 | varied |
| Silicon nitride | 2.04 | -0.0002 | 30 nm |
| Silicon wafer | 5.47 | -2.99 | inf |
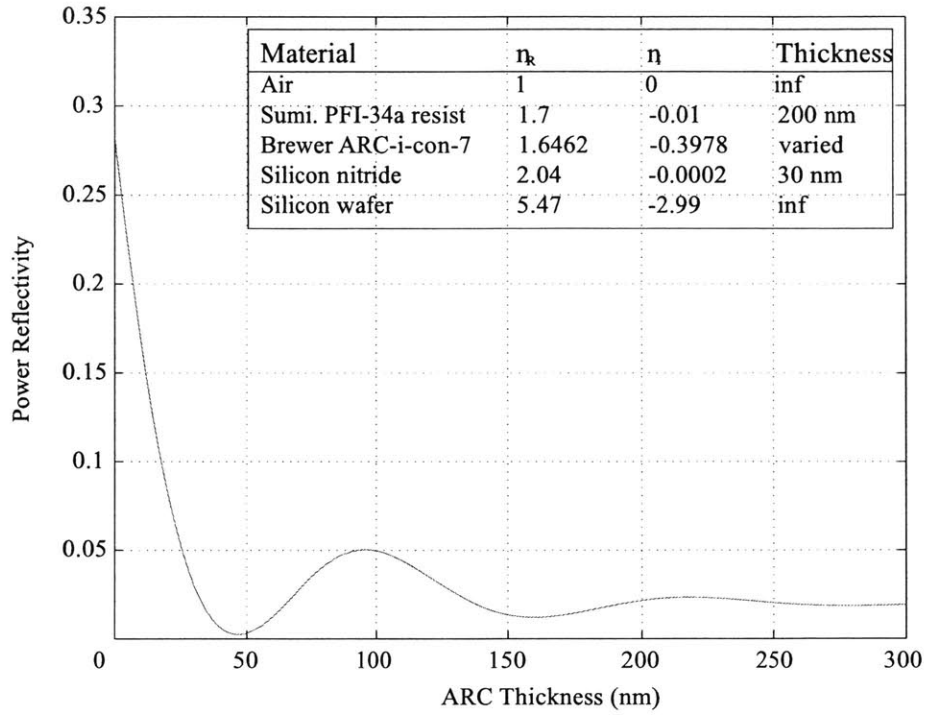
Figure 3-2: Simulated reflectivity at the resist/ARC interface as a function of ARC thickness.
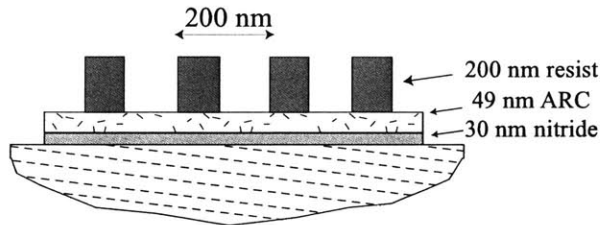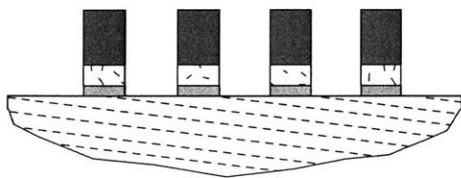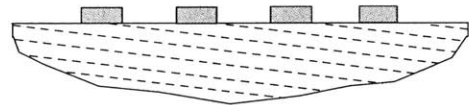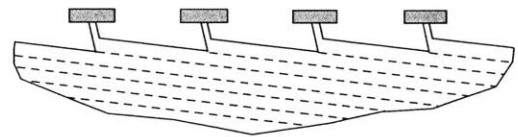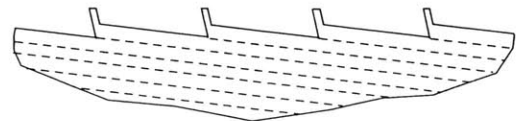


Figure 3-3: Fabrication process diagram for 200 nm-period grating with $7^o$ blaze angle.

### 3.4.1 Interference Lithography

The wafer used in this process has the its surface normal rotated $7^o$ from the [111] direction along the [1$\bar{1}$0] axis, as previously described. The wafer is prepared by coating 30 nm of silicon nitride by chemical vapor deposition, then spinning 49 nm of ARC and 200 nm of photoresist.

To achieve 200 nm-period, the beam half angle of the interference lithography apparatus is set to be approximately $61.4^o$ for $\lambda = 351.1$ nm. The image grating lines are aligned to the [1$\bar{1}$0] axis, which is perpendicular to the provided primary wafer flat. Accurate alignment is achieved by cleaving a sample, and adjusting to an angular offset characterized by the moiré pattern experiment explained in Chapter 2. A dose of 24.8 mJ/cm$^2$ was used to achieve a line to space ratio of one. A micrograph of the exposed resist grating after developing is shown in Figure 3-4. The height of the resist grating has been reduced, so some of the resist on the top was exposed. This is due to a mismatch of intensities between the two beam arms, resulting in non-perfect contrast. Environmental disturbances such as ground vibration and air turbulence might also affect contrast.

### 3.4.2 Pattern Transfer

After the grating has been defined in resist, the pattern has to be transfered down to the nitride etch mask layer. This pattern transfer is done by RIE. To etch the organic ARC film, oxygen is used as the reactive species. A flow rate of 45 sccm, a low pressure of 1.4 mTorr, and a power of 25 W are used as parameters. Low pressures are used so that the mean free path of the ions will be smaller, and thus the etch will be vertical. Higher pressure increase the collision of the charged ions and the etch will be less directional. The wafer is etched for about 4.5 minutes, and the resulting profile is shown in Figure 3-5(a).

After the grating is transfered down to the ARC layer, a CHF$_3$ RIE is used to etch into the nitride mask. The CHF$_3$ RIE was operated at 10 sccm, 20 mTorr, and 100 W for 3 minutes. The resulting profile is shown in Figure 3-5(b). After the silicon
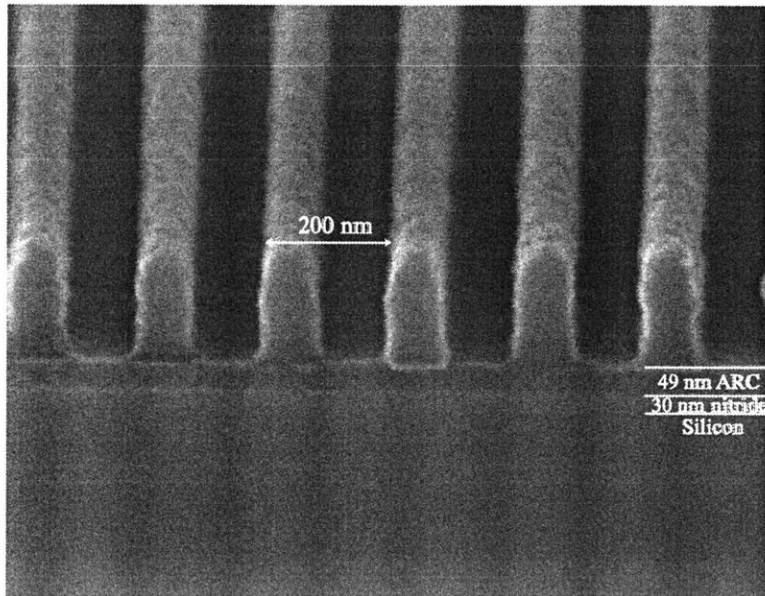
Figure 3-4: Cross-section micrograph of 200 nm-period resist grating after exposure and developing.
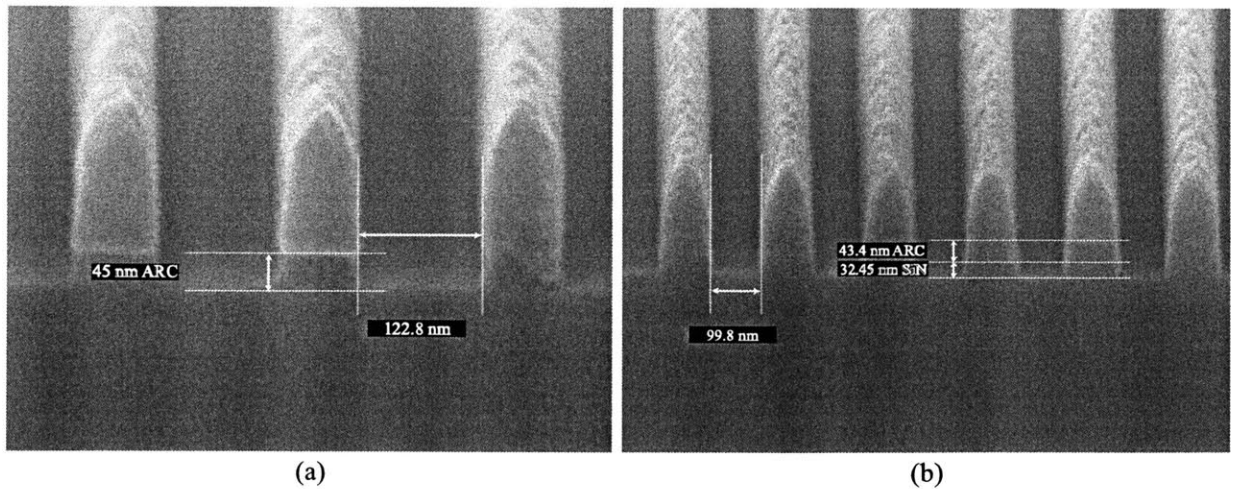


Figure 3-5: Cross-section micrograph of wafer after, (a) 4.5 minutes of oxygen RIE, and (b) 3 minutes of CHF$_3$.
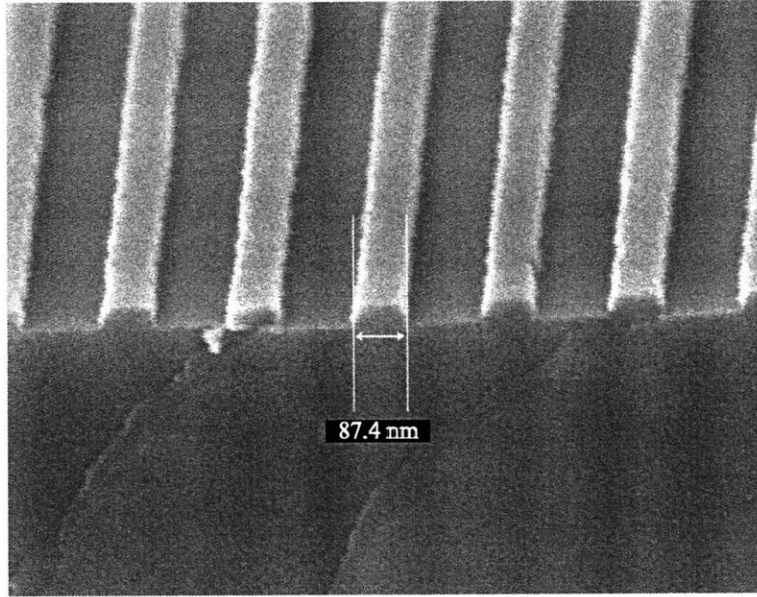
Figure 3-6: Cross-section micrograph of silicon nitride mask after RCA clean.

nitride has the grating pattern etched through, the ARC and resist stack are not needed anymore. In an RCA clean step all the remaining ARC and resist are cleaned, along with any other polymer material from the $CHF_3$ etch process. The wafer now only contain silicon with a nitride mask (Figure 3-6). The wafer is ready for KOH wet anisotropic etching.

### 3.4.3 Anisotropic Etching

At room temperature, silicon readily oxidizes. Thus on silicon surfaces there is always a layer of native oxide that has thickness in the order of nm. The native silicon oxide layer protects the silicon from KOH etching. Thus before etching in KOH, the wafer must be dipped in buffered HF for about 15 seconds to remove the oxide layer.

The KOH bath used is 20% by weight, and the wafer is etched at room temperature. It usually takes very little time for the profile to be etched. Once the blazed profile has been etched in the KOH bath, the area with the pattern will appear darker. This is because the reflectivity of the blazed profile is lower than for a flat surface. Further etching in KOH can be used to reduce the line-width of the grating, resulting
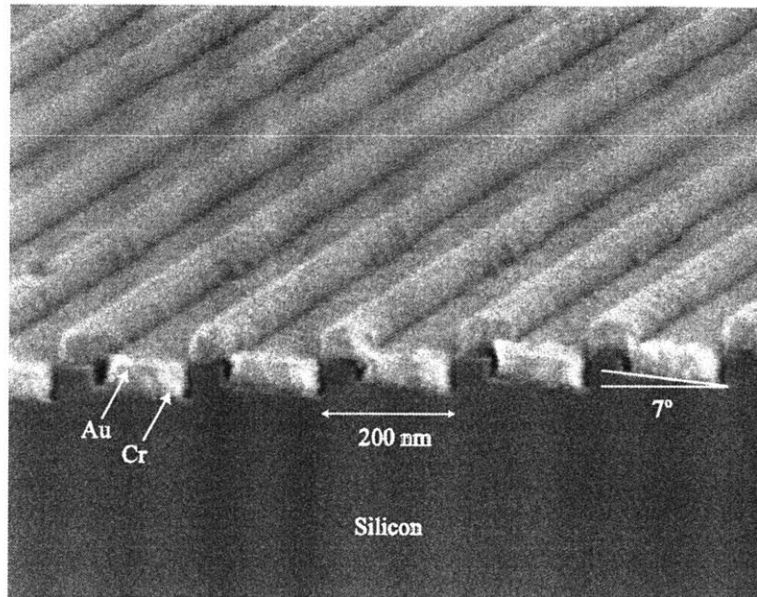
Figure 3-7: Cross-section micrograph of completed 200 nm-period grating with $7^o$ blaze angle.

in more blazed facet area. After being etched in KOH, the silicon nitride mask can be removed in concentrated HF. The completed profile is depicted in Figure 3-7. In this case the grating was coated with 5 nm of chrome and 40 nm of gold to increase x-ray reflectivity.

The under-cut etch rate of the KOH is a good indication of the accuracy of the alignment. Since the etch rates are so different for given directions, a slight angular misalignment can lead to big differences in etch rates. In an experiment two wafers are off-aligned purposely by $1^o$ and $2^o$. The under-cut rates are found to be 0.92, 1.53, and 2.96 nm/min for $0^o$, $1^o$, and $2^o$ misalignments, respectively. The plotted trend can be seen in Figure 3-8. These results are preliminary, but the general trend can be seen. At a $2^o$ misalignment the under-cut etch rate is tripled. With more experiments, a given under-cut etch rate would be able to give quantitative information on the misalignment.
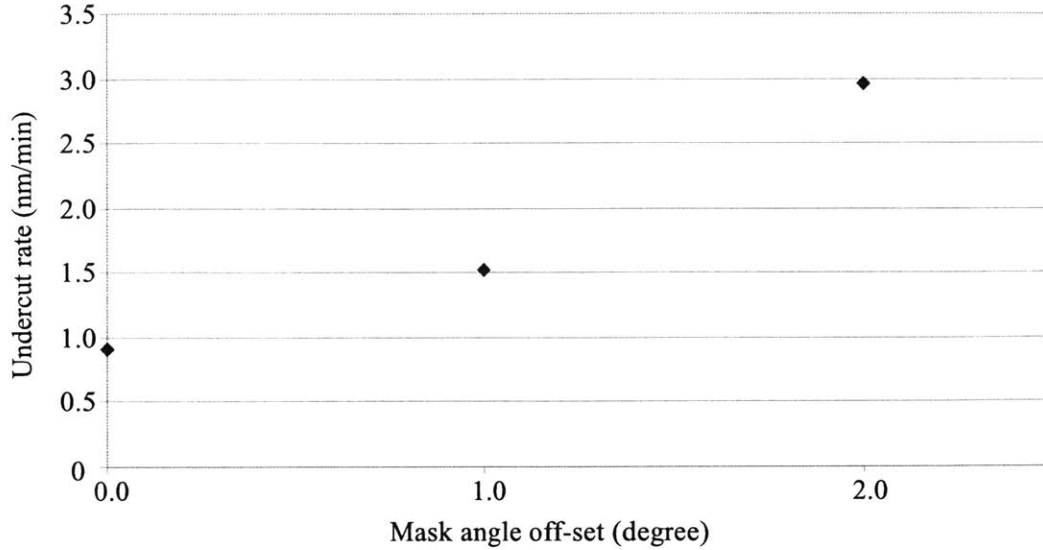
Figure 3-8: The effects of misalignment on under-cut etch rates.

## 3.5 Grating Line-width Control

For blazed diffraction gratings the efficiency is related to the area of the blazed facets. Therefore it is desired to increase the blazed areas by reducing the grating line-width. There are two methods in which the line-width can be controlled, over-exposure during lithography, and over-etching during KOH.

Over-exposure of resist is able to reduce the grating line-width. The reduced line-width will be transferred through the process and the finished grating will have increased blazed facets. Figure 3-9 depicts the resist profile for dose of (a) 27, (b) 31, (c) 40, and (d) 44 mJ/cm$^2$.

However lithography dose is not the ideal parameter when trying to reduce the line-width to below 50 nm. First of all the resist grating patterned with interference lithography has high line-edge-roughness, partly due to the fringe jittering during exposure. When the width of the line is reduced to less than 50 nm, the resist usually collapses because it is not mechanically stable due to surface tension of water. Also the time needed for high dose is twice as long as for regular dose. Long exposure time makes the interference lithography setup more vulnerable to environmental disturbances.
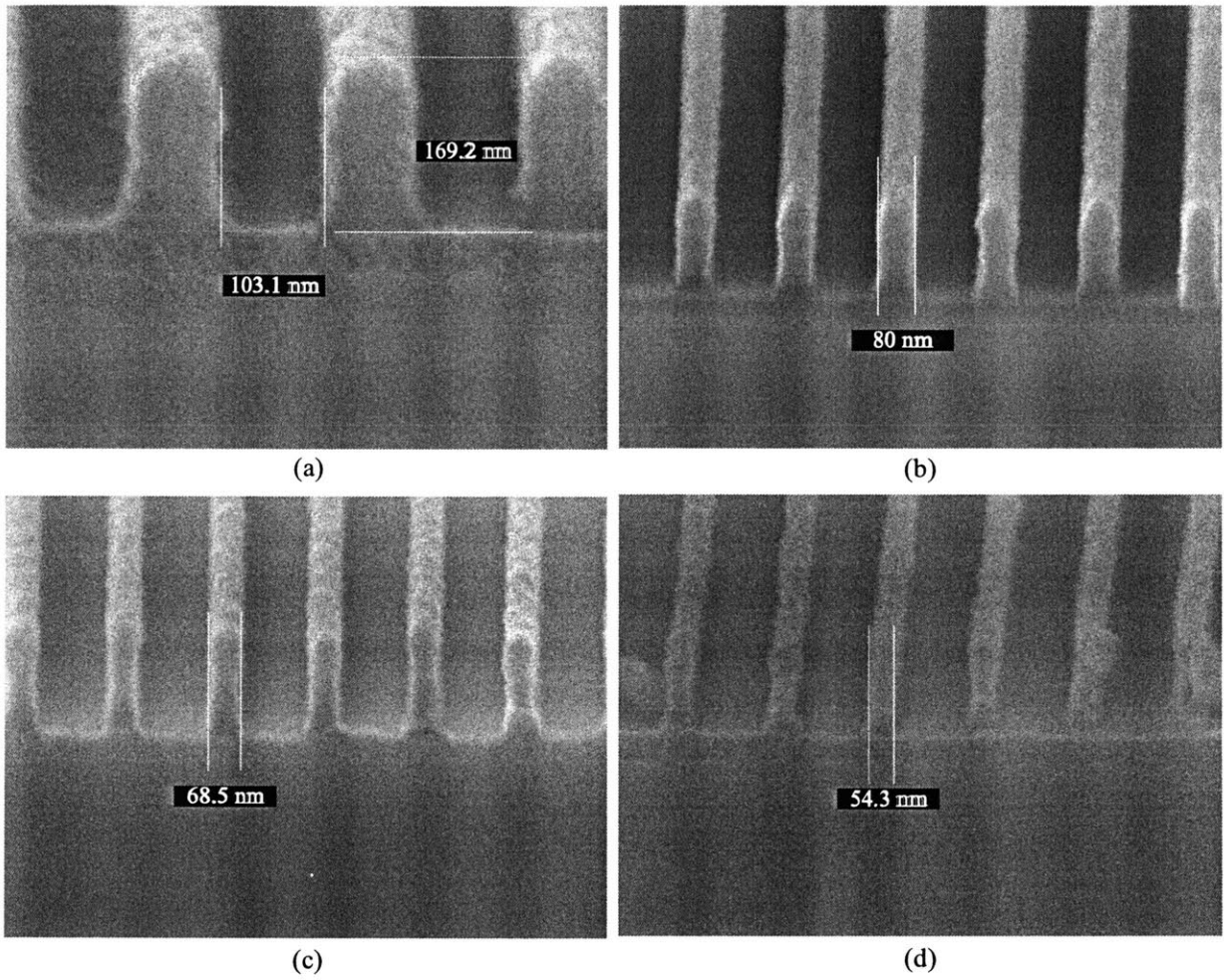
Figure 3-9: Resist profile for dose of (a) 27, (b) 31, (c) 40, and (d) 44 mJ/cm$^2$.
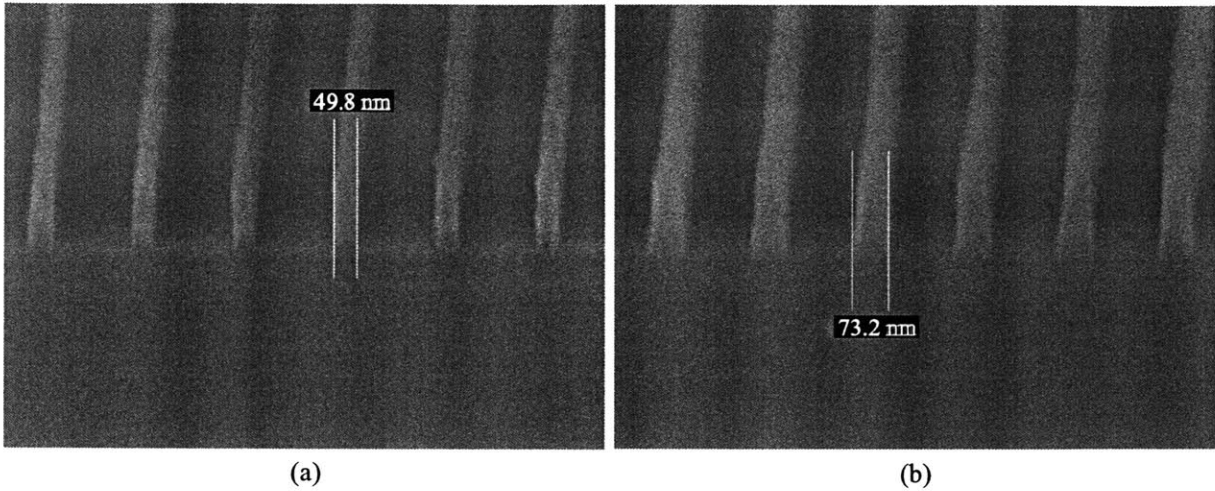
Figure 3-10: Cross-section micrograph of grating with increased line width (a) before, and (b) after CHF$_3$ RIE.

Also when plasma etching with CHF$_3$ RIE for structures in the order of nanometers, the line-width can not be well controlled. RIE with CHF$_3$ is known to form a fluorocarbon polymer. This material deposits inside the chamber and on the wafer. The fluorocarbon that forms in the bottom of the trenches does not produce a problem, since it is physically sputtered away by the ions. However the polymer deposits on the sidewalls is hard to be sputtered away, and thus the resist line-width increases. This effect became a problem during an experiment to reduce the line-width, as shown in Figure 3-10, where the width of the line increased from 49.8 nm to 73.2 nm.

The profile also has a sloped wall, instead of the vertical wall before the etch. Other gas species can be used to etch silicon nitride, one of the most popular being CF$_4$. However, in our application CF$_4$ has an even more severe problem. Since CF$_4$ etches both silicon and silicon nitride, the etching will not stop at the nitride/silicon interface. This is critical because if the etching continues into silicon, during the KOH step the etching will undercut immediately and result in undesirable profile. Therefore CHF$_3$ is still used for the etching of silicon nitride. The deposition of the hydrocarbon material during CHF$_3$ RIE makes the smallest line-width around 70 nm.

Another method to achieve thin lines is to undercut the silicon nitride mask during
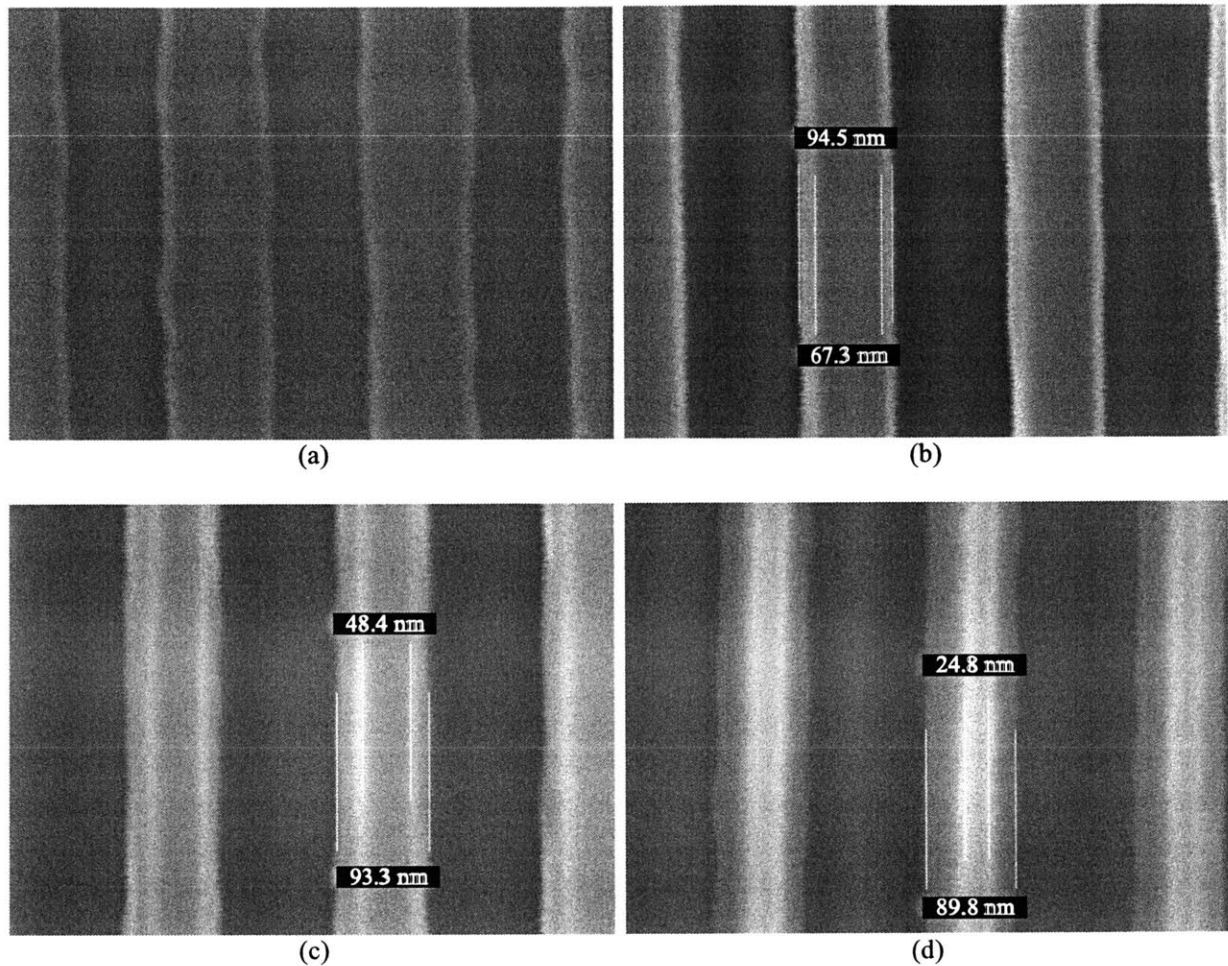
Figure 3-11: Top view SEM of KOH underetching for (a) 0, (b) 15, (c) 25, and (d) 38 minutes. Cross-section schematic is illustrated in Figure 3-3(d)

KOH etching. This process is more ideal for line-width control since the undercut rate is relatively slow. Without etching the nitride mask, the line-width of the grating can be monitored using a SEM. Using a higher acceleration voltage ($\sim$ 10kV), the electrons will be able to penetrate through the 30 nm of nitride mask. Figure 3-11 depicts the line-width of the grating after (a) 0, (b) 15, (c) 25, and (d) 38 minutes. The line-edge-roughness caused partly by environmental instability during lithography exposure can be observed.

The smallest grating line-width etched is around 25 nm. Theoretically this width can be reduced more, but the limiting factor is the dose uniformity during lithography.

<div align="center">(a)          (b)</div>
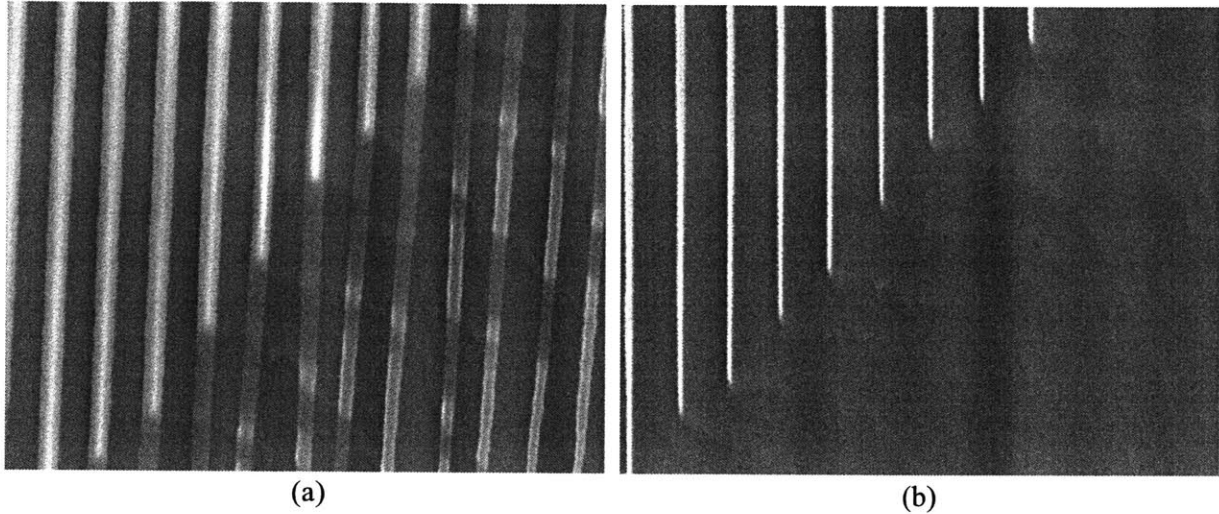
Figure 3-12: Top view SEM of collapsed structures (a) before and, (b) after silicon nitride mask removal.

Using the traditional interference lithography setup the intensity of the two spherical waves is position dependent. A line-width decrease of 20 nm can be observed between at the center of the wafer and at 15 mm of vertical displacement. A decrease of around 10 nm is observed at 15 mm of horizontal displacement. With such a large amount of line-width variation, undercutting to less than 25 nm might have cause structural collapse at other places. Figure 3-12 is taken from the same sample as Figure 3-11(d), and it illustrates collapsed gratings due to dose variations.

The collapsed structures resulted in a lift-off of the silicon nitride mask. Since the nitride grating mask was not attacked by KOH, it is still connected to the silicon wafer. At the blazed facets terraces can be seen. This is because the grating lines collapsed one by one, and the blazed facets are still preserved.

The fundamental sources of error for line-width control are the dose uniformity and the interference fringe stability. These limiting factors are embedded in the interference lithography exposure, and are hard to eliminate. For better line-width control patterning of the grating via the NanoRuler [6] [18] will be necessary. For the existing setup the smallest line-width achieved is around 25 nm.

# 3.6 Grating Profile

The grating profile geometry and smoothness will give a direct implication of the diffraction efficiencies of the grating. An image scanned with an Atomic Force Microscope (AFM) is shown in Figure 3-13. Figure 3-13(a) illustrates a 3-dimensional view, while Figure 3-13 shows the cross-sectional profile. The smoothness of the blazed (111) facets can be observed. The RMS roughness of the blazed surface is found to be $\sim$0.15 nm[1] in a scanned area of around 50 by 50 nm$^2$. The AFM tip used is a super-sharpened silicon tip with tip radius less than 5 nm and half cone angle less than 10$^o$ for the last 200 nm.

Several artifacts are visible in the AFM image shown in Figure 3-13. Most of these are caused by the finite geometric dimensions of the AFM tip. The edge rounding effects can be seen readily at any sharp corner, and areas that have negative angles are hidden. The image can be seen as a convolution of the actual profile with the physical geometry of the tip. The AFM resolution is limited when the dimensions of the sample to be scanned approaches the dimension of the tip. However the AFM is useful in giving statistical measurements of the RMS roughness for the (111) facets.

The silicon ribs that result from the etch mask might be problematic depending on the mount type for x-rays. X-rays reflects only at small incident angle, resulting in grazing-incidence reflection. If these anisotropic etched gratings are used as in-plane gratings, where the incident beams are parallel to the grating lines, the silicon ribs will block the x-rays. If used as off-plane gratings, where the incident beams are perpendicular to the grating lines, the symmetric ribs will reduce the effect of the blazed facets.

Further processing can remove these ribs, if needed, by a lift-off process[12] as depicted in Figure 3-14. After anisotropically etching the wafer in KOH, evaporate a thin film of Cr with the nitride mask still protecting the silicon ribs. Due to the height difference between the nitride mask and the blazed facets, there will be discontinuities

---

[1]The RMS noise measurement is limited by the noise level of the AFM. The noise for the system used has noise of $\sim$0.1 nm. The AFM noise study will be explained further in Appendix B.
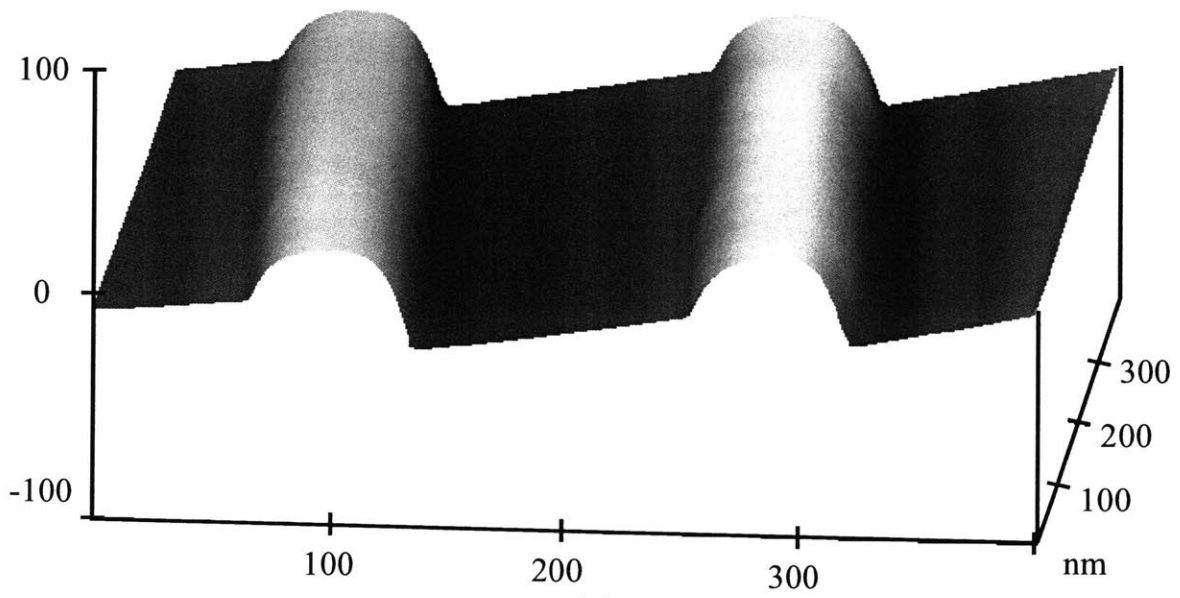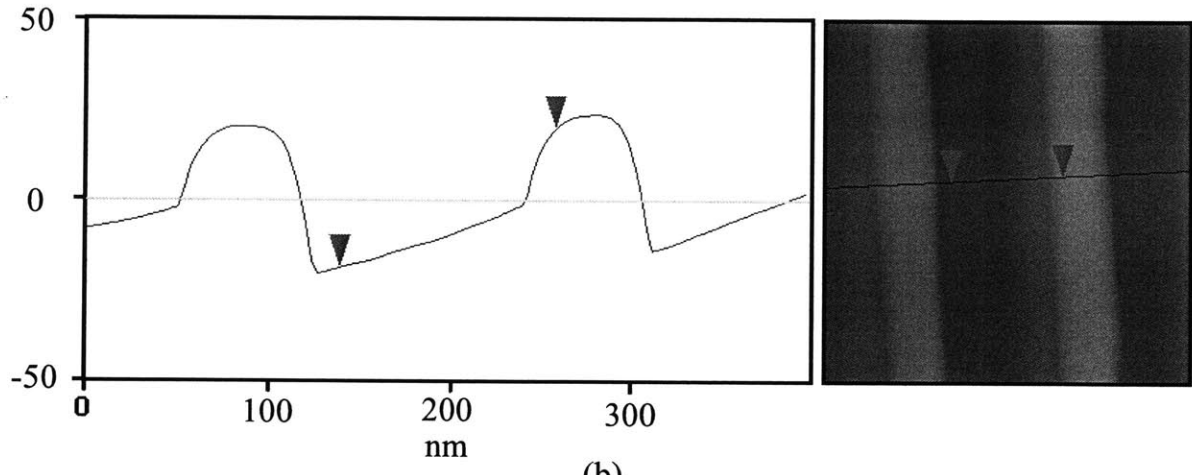
Figure 3-13: (a) 3-D, (b) cross-section atomic force micrograph of the 200 nm-period blazed grating.

(a) Anisotropically etched in KOH.

(b) Evaporate thin Cr.

(c) Lift-off by etching nitride with HF.

(d RIE with CF$_4$

(e) Remove Cr mask with wet etchant.
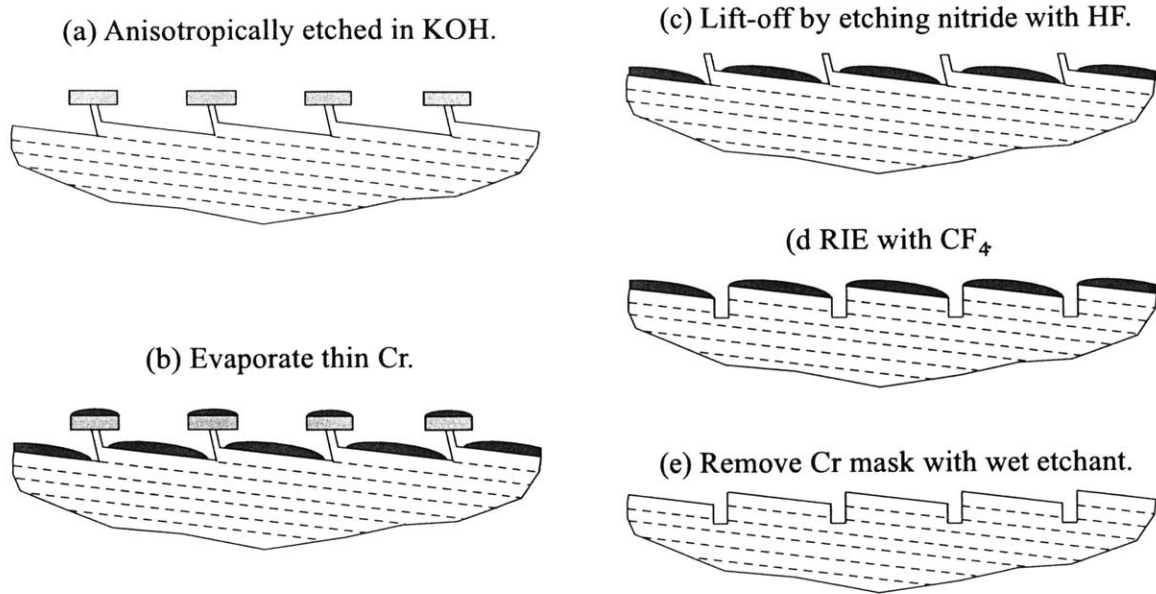
Figure 3-14: Lift-off process to remove silicon ribs.

in the Cr film. When the wafer is submerged in HF, these discontinuities will allow the nitride to be etched, resulting in the lift-off of the Cr above. With the Cr film protecting the blazed facets, the silicon ribs can be etched in CF$_4$ RIE. After the ribs are etched, the Cr protection film can be removed in a Cr wet etchant. The resulting profile should resemble Figure 3-14(e).

## 3.7  Conclusion

Using interference lithography, off-cut silicon wafers, and anisotropic etching, 200 nm-period gratings with $7^o$ blaze were successfully fabricated. The RMS roughness of the resulting (111) blazed facets is less than 0.2 nm. The line-space ratio is optimized to achieve larger blazed facet areas, and the silicon ribs are reduced to a width of around 25 nm. The line-width can be further reduced if the dose uniformity can be better controlled. The performance of the anisotropically etched silicon blazed gratings will be covered in Chapter 6.

# Chapter 4

# Grating Replication with Nanoimprint Lithography

## 4.1 Introduction

The anisotropic etching process described in Chapter 3 is able to fabricate blazed diffraction gratings with desired surface profile and extremely low roughness. These near atomically smooth surfaces will minimize undesirable scattering, thus increasing diffraction efficiency. However, the dependency of the grating profile on the crystal lattice direction makes it essential to use specially oriented wafers. Therefore this process is relatively expensive and time consuming. The grating area required by NASA's x-ray space telescope mission *Constellation-X* is in the order of 100 square meters. To facilitate the blazed grating fabrication process, a replication procedure nanoimprint lithography (NIL) will be investigated. The feasibility of replacing the fabricated silicon blazed grating with NIL replicated grating will be the primary motive.

## 4.2  Nanoimprint Lithography

NIL is a mechanical replication process in which a viscous polymer solution is pressed against a mold[1] to form a desired shape. The polymer will then be cured or treated, so that the polymer chains will cross-link. After separation, the result is a polymer replication with an inverted profile.

NIL operates on the fundamental principles of the molecular structure of polymers. Polymers consist of covalently bonded chains, and weaker secondary bonds between the polymer chains. When the secondary bonds between the chains break at the glass transition temperature, the polymer will soften. The viscosity of the softened polymer is dependant on the occasional covalent bonding that cross-links the polymer chains. In the absence of these covalent bond cross-linking, the polymer will turn into a liquid. The principle of NIL is to break the secondary bonds of the polymer so that the material can conform to the shape of the master. When the liquid polymer fills all the spaces, the polymer chains are cross-linked, forming a glassy material.

For NIL the separation between the master and the polymer imprint is critical. Since silicon exhibits high adhesion energy [21], a thin film of a low surface energy material such as fluorocarbon is needed to promote release. First, any organic contaminants adsorbed on the surface of the mandrel were cleaned in an UV/ozone chamber for 3 minutes, and then tridecafluoro-1,2,2,2-tetrahydrooctyltrichlorosilane (FOTS) is formed over the master by vapor evaporation.

The vapor phase deposition is done in a low vacuum dessicator, since the reducing the water molecules in the bulk phase will increase the quality of the film. The setup can is shown as Figure 4-1. A thin alkylsilane monolayer film will form readily on the master surface, and it is cured at 100 $^{o}$C for 5 minutes. Fluoroalkysilane coated surface exhibits adhesion energy less than 20 $\mu J/m^2$, four orders of magnitude less than that of silicon with native oxides ($\sim$100 $mJ/m^2$).

There are several methods that can initiate the formation of the secondary bonds

---

[1]The mold is the physical pattern that the imprint process is replicating. Will be referred to as the master/mandrel.
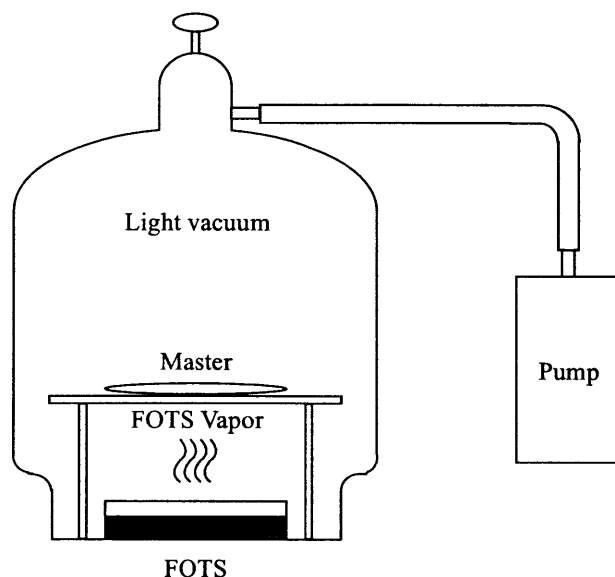
Figure 4-1: The setup for vapor phase deposition of FOTS film.

to cure the polymer. The two most popular are the thermal-cure process purposed by Chou *et al.* [7], and the UV-cure process purposed by Bailey *et al.* [1]. The thermal-cure utilizes a thermal cycle as the mechanism to break and reform the secondary bonds. Figure 4-2 depicts the thermal-cure process. A polymer material such as polymethylmethacrylate (PMMA) is first spun on a blank substrate. The coated substrate is then heated above the polymer's glass transition temperature, so that it turns into liquid phase. The treated master is pressed into the liquid polymer, and then cooled to room temperature. After separation the imprint substrate will have the inverted master profile in polymer.

The UV-cure process is also commonly known as the step and flash imprint lithography (SFIL). It uses a UV-curable liquid that is inviscid as the conformable material. Figure 4-3 depicts the UV-cure process. The liquid UV-curable polymer[2] is dispensed onto a transparent template. The treated master is pressed onto the template, and the low viscosity liquid will be shaped. When exposed to UV radiation, the photo initiator will start a chemical reaction, and cross-link the polymer chains. When enough UV energy is absorbed by the polymer, it will be fully cured to a solid material.

---

[2]The UV-curable polymer is formulated as described by Bailey *et al.* [2]
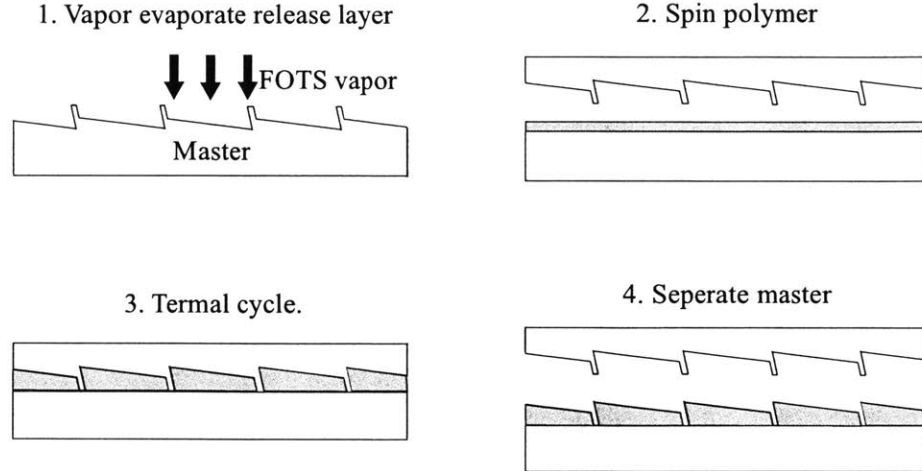
Figure 4-2: The thermal-cure NIL process: (a) Master is treated with FOTS, (b) a polymer is spun onto the imprint template, (c) thermal cycle to break and form the secondary bonds, and (d) separated imprint has an inverted master profile.

The advantage of this process over thermal-cure is that it can be done at room temperature, thus eliminating and possibility for stress induced by thermal mismatch. However for the UV-cure process either the imprint master or template has to be transparent at the UV spectrum, so that the polymer can be cured.

## 4.3 Imprinting 400 nm-period Inverted Triangular Grating

NIL has demonstrated replicating sub-50 nm-period structures with little distortion. Integrating NIL into the anisotropically etched grating might yield a more time and cost efficient process. However most of the literature on NIL results are imprints from 2-dimensional patterns. Blazed gratings have simple 3-dimensional structures, since the blazed profile and smooth surface must be preserved. Therefore several samples were imprinted and characterized, with the imprinted profile fidelity and surface roughness as the primary factors to examine.

The initial imprint experiment used the anisotropically etched 400 nm-period

**1. Vapor evaporate release layer**

FOTS vapor

Master

**2. Deposite liquid polymer**

polymer

UV-transparent template

**3. Cure with UV light**

UV Light

**4. Seperate master**
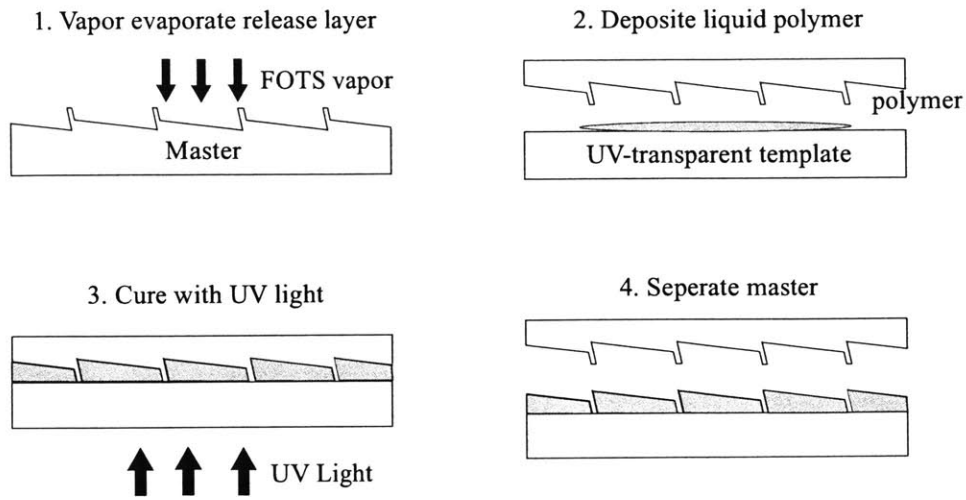
Figure 4-3: The UV-cure NIL process: (a) Master is treated with FOTS, (b) an UV-curable liquid is dispensed onto the transparent imprint template, (c) UV radiation to cross-link the polymer chains, and (d) separated imprint has an inverted master profile.

UV radiation

Fused silica wafer

Flexure

UV-curable polymer

Vacuum pump
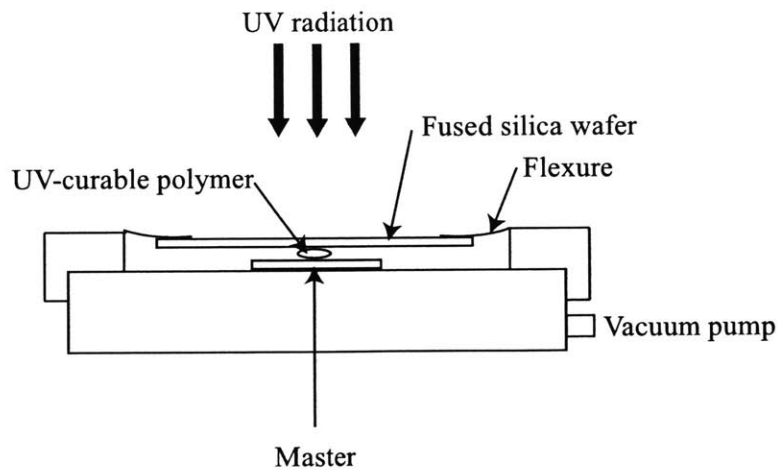
Master

Figure 4-4: UV-cure NIL setup for replicating the 400 nm-period inverted triangular grating.

inverted triangular silicon grating, similar to the 200 nm-period grating shown earlier as Figure 2-4 in Chapter 2, as the master [5]. The UV-cure NIL process is used to replicate the triangular profile. Since the master used is (100) silicon, an UV-transparent template made of fused silica is used. The master is die-sawed into an area of ~40 by 20 mm$^2$. The NIL imprint setup is shown in Figure 4-4. The master is situated at the bottom on a rubber flexure. A drop of UV-curable liquid polymer is dispensed on the master, and then covered with a fused silica wafer. The master-wafer stack is then covered with another rubber flexure, to create an sealed environment. A vacuum pump then pumps the air out, thus forcing the two rubber pieces onto each other. The light vacuum enhances direct contact between the master and the imprint template. UV light ($\lambda \sim 400$ nm) is exposed from the top, and cures the polymer with a dose of 100 mJ/cm$^2$. The master and the imprint substrate are separated by hand.

The replicated gratings show excellent surface uniformity over the area that was imprinted. No apparent release damage was observed over the imprinted area. An image of the replicated 400 nm-period inverted triangular grating was scanned using an AFM and is shown in Figure 4-5. The replicated grating exhibits an inverted profile of the mandrel with high conformity. The occasional spikes on the surface are noise artifacts.

The rounded edges shown on the AFM images may be artifacts due to the tip's finite dimension. SEM images of the same imprinted grating show sharp edges (Figure 4-6). The small ripples at the bottom of the imprinted gratings may be caused by the elasticity of the material. Since the ripples are perpendicular to the grating line direction, they could be the result of the polymer stretching and springing back during cleaving of the sample. The micrograph was taken at close proximity to the cleaved edge.

Even though the imprinting results are encouraging, there are some factors limited the imprinted fidelity of the gratings. First of all there are some apparent asymmetry of the imprinted triangular gratings. This may be scanning artifacts due to the tip, which was a multi-wall carbon nanotube mounted on a silicon tip. The nanotube's
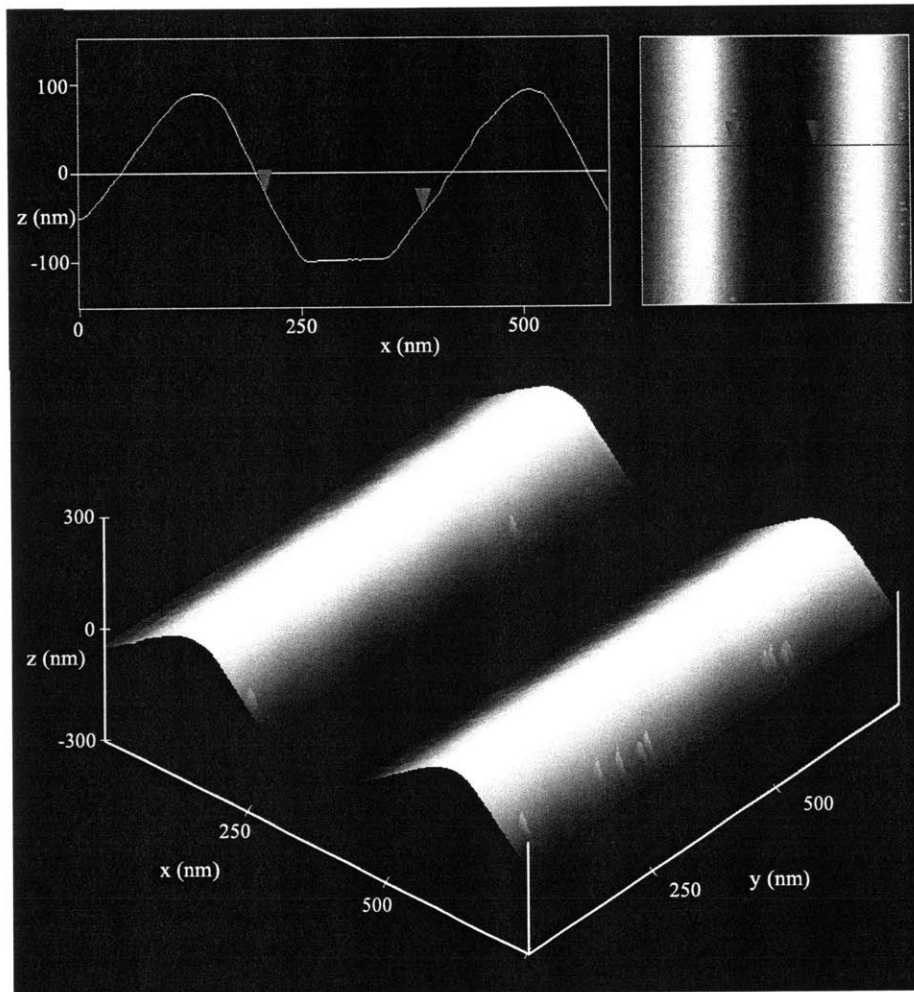
Figure 4-5: AFM image of imprinted 400 nm-period inverted triangular grating. (a) Cross-section view, (b) 3D view.
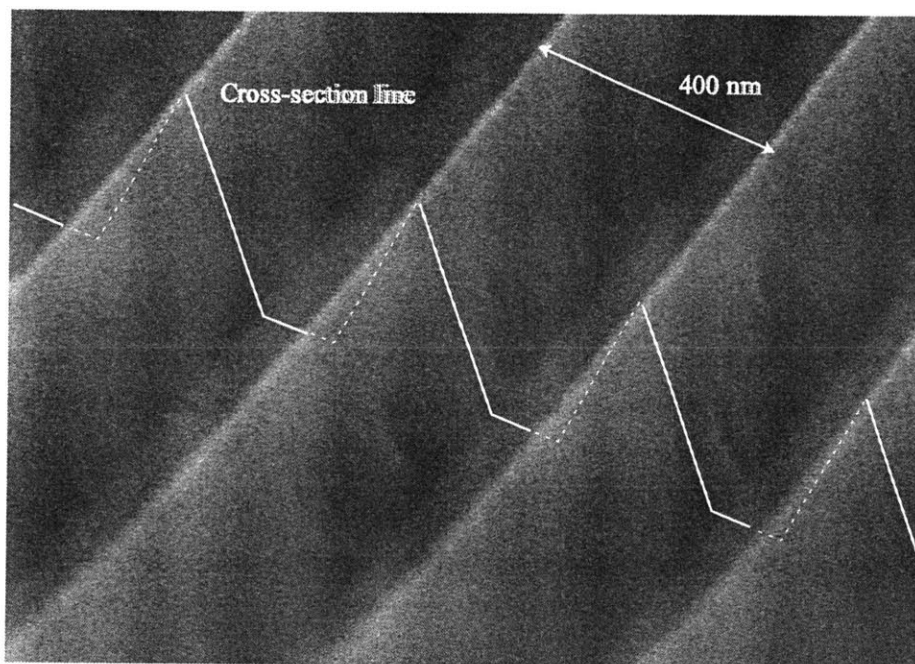
Figure 4-6: SEM image of imprinted 400 nm-period inverted triangular grating. Sharp edges can be observed. The slight ripples at the base of the triangles may be the result of cleaving.

angle from the vertical has a $\pm 10^o$ specification, given by the vendor. The asymmetry might also be real, in which the elastic polymer was deformed during manual separation. In addition, the residual layer was not properly controlled in the imprinting setup, resulting in very thick films. These ambiguities can be resolved by using a better controlled setup.

## 4.4 Imprinting 200 nm-period Grating with $7^o$ Blaze

After encouraging results from preliminary imprints of the 400 nm-period inverted triangular gratings, the 200 nm-period gratings with $7^o$ blaze, fabricated as described in Chapter 3, were also imprinted. Imprinting the blazed gratings is more problematic due to the shadowed negative angles ($\sim 13^o$). To achieve optimum imprinting condition, this imprint experiment was done in collaboration with Nanonex Corporation[3], a commercial NIL vendor.

The limiting factors were better controlled in a commercially ready NIL system. The blazed grating was imprinted over a 100 mm diameter area in a thermal-cure process. The imprint conditions were at a temperature of $120^oC$ and pressure of 200 psi by the NX-1000 Nanoimprintor. The cross-section micrograph is shown in Figure 4-7.

The cross-section profile shows excellent imprint fidelity. The residual polymer layer is well controlled to around 200 nm. The blazed angle is well preserved, and the groove edges is apparently sharp. Local charging by the electron beam is partly responsible for the glow at the groove edges, which blurs the micrograph. The profile can also be characterized by an AFM, as shown in Figure 4-8. The sharpness of the edge is again limited by the physical tip radius, which is in the order of 5 nm[4]. Notice that AFM artifacts arise at shadowed angles, and the SEM image is a better representation of the general profile.

---

[3]Nanonex Corporation, 1 Deer Park Drive, Suite O, Monmouth Junction, NJ 08852, http://www.nanonex.com

[4]AFM tip used is a super-sharpened silicon tip, with radius less than 5 nm and half cone angle less than $10^o$ at the last 200 nm of the tip. Purchased from Molecular Imaging
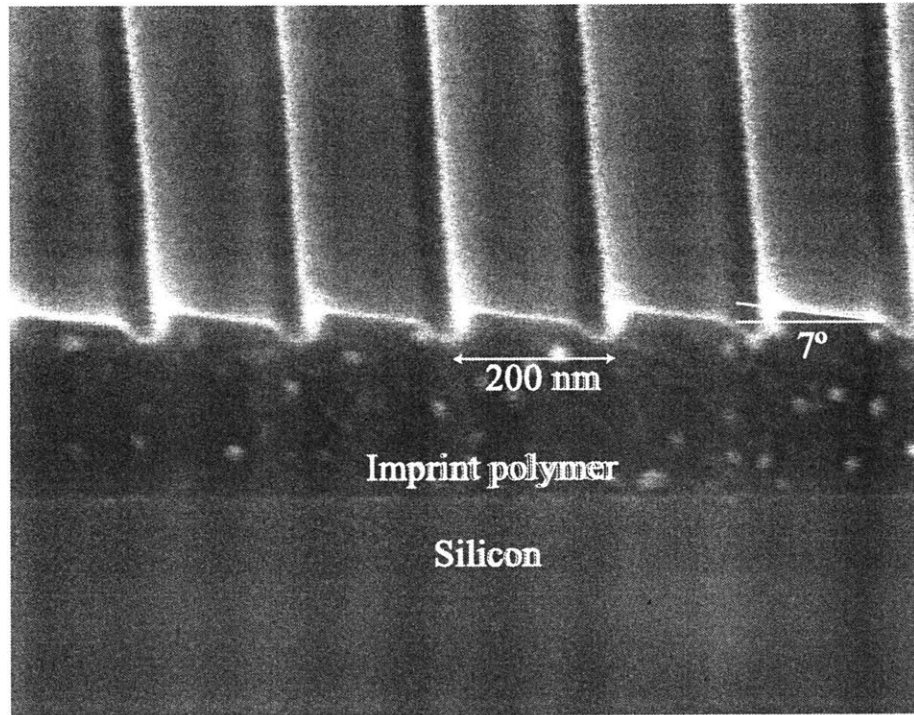
Figure 4-7: SEM image of imprinted 200 nm-period grating with 7° blaze.
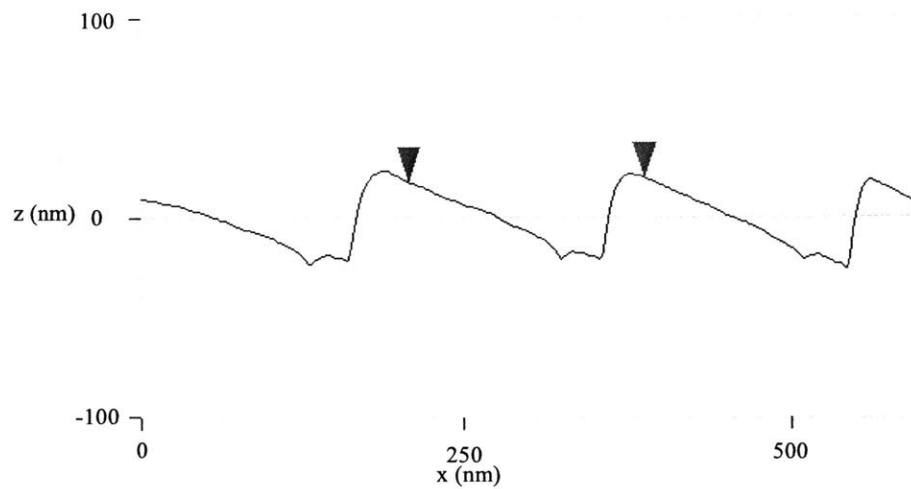


Figure 4-8: Cross-section profile AFM image of imprinted 200 nm-period grating with 7° blaze.
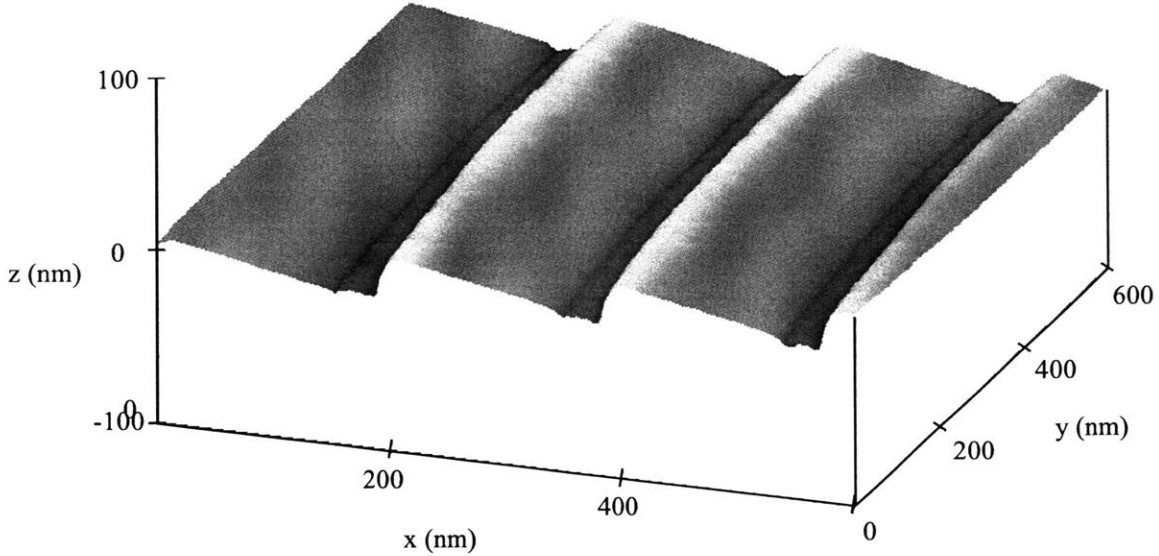
Figure 4-9: 3D AFM image of imprinted 200 nm-period grating with $7^o$ blaze.

The 3-dimensional AFM image illustrated in Figure 4-9 shows the surface quality of the imprinted grating. The blazed facets are well preserved, and from visual inspection the smoothness is close to that of the master. The RMS roughness of the blazed facets is scanned by AFM and is less than 0.2 nm, which is in the same order as the master grating. The apparent curvature of the grating lines is due to non-linearity in the piezoelectric tube, which scans the surface.

## 4.5 Profile Comparison

As described earlier in Chapter 3, the silicon posts that remained from the silicon nitride etch mask can be problematic, and can be removed with further processing. If the fabricated silicon blazed grating is to be used for diffraction, the posts would be removed. However, since imprinted gratings have an inverted profile, blazed gratings with the silicon posts is a better replication master. Figure 4-10 illustrates this point from a simple geometric perspective for an off-plane mount. If the silicon posts on the master are etched in a lift-off process, then the imprinted profile would have extruded
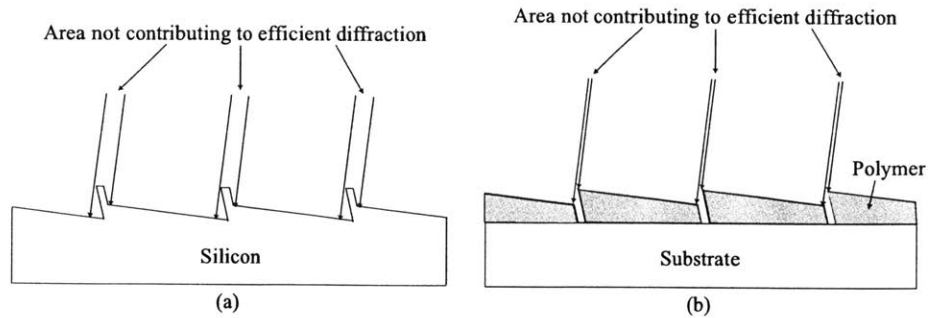
Figure 4-10: Grating profile and area not contributing to efficient diffraction for (a) the silicon master grating, and (b) the imprinted grating.

posts. For the case when the blazed master has the silicon posts, the imprinted grating will have more effective area for diffraction.

## 4.6 Conclusion

Using NIL as a process to replicate simple 3-dimensional gratings yields encouraging results. 400 nm-period gratings with an triangular profile and 200 nm-period gratings with $7^o$ blaze angle were successfully replicated by NIL over a 100 mm wafer. The imprinted gratings demonstrate high profile conformity, and the blazed facets have RMS roughness less than 0.2 nm. By using replications instead of anisotropically etching every grating, enormous time and money are saved. The performance of the replicated polymer blazed gratings will be covered in Chapter 6.

Even though NIL is able to replicate the geometric profile of the blazed gratings with high conformity, the material properties of polymer gratings are of concern. The stiffness of polymer materials are in the range of 1-3 Gpa, two orders lower than that of silicon. There are vibrational and thermal issues that occurs during space flight. The question of whether the polymer gratings will physically survive the trip to space remains unanswered.

# Chapter 5

# Thin Film Stress Analysis with Zernike Polynomials

## 5.1　Introduction

In previous chapters extensive details have covered the fabrication process for blazed diffraction gratings. For both the anisotropically etched silicon gratings (Chapter 3) and the imprinted polymer gratings (Chapter 4), a thin layer of Au needs to be coated for x-rays to reflect effectively by grazing incidence. During deposition, these thin films usually develop internal stress, which will strain the wafers and add out-of-plane distortion. For some applications such distortions are critical. For example, the x-ray diffraction gratings used for NASA's x-ray telescope *Constellation-X* will need the optic flatness to be lower than 0.5 $\mu$m across 100 mm area. Therefore it is extremely important to analyze the coated thin film stresses and its out-of-plane distortions.

To order to study the out-of-plane distortions caused by film stress, a Shack-Hartmann wavefront metrology tool[1] is used to map the 2-dimensional wafer surface profile. By comparing the surface map of the wafer before and after depositing the metal film, the out-of-plane distortion can be found. However, it is difficult to compare directly the height information of the two surface maps. Another method, the

---

[1]Detailed information of the Shack-Hartmann system is described in Forest *et al* [11].
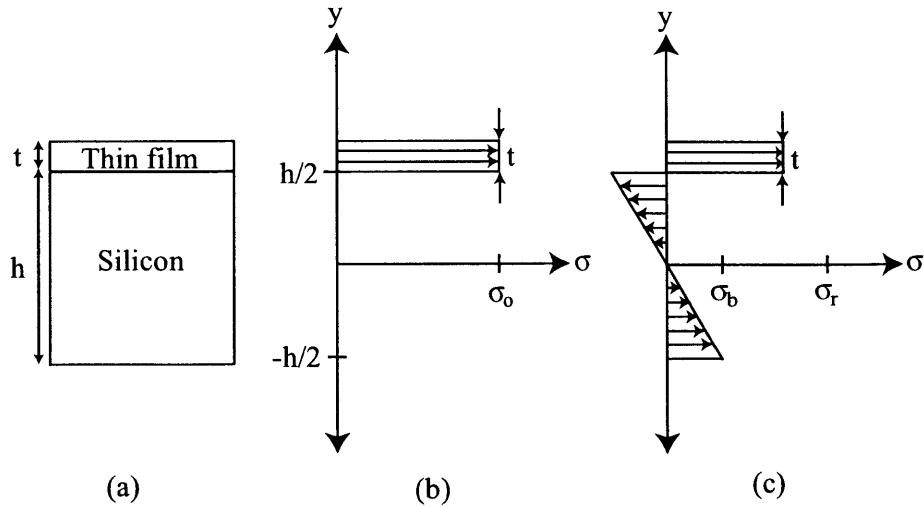
Figure 5-1: (a) Cross-section of a thin film on a wafer, and its residual stress (b) before release and bending, and (c) after release and bending.

comparison of the Zernike coefficients, can quantitatively analyze all modes of surface distortions. In this chapter the quantitative analysis of film stress using the Zernike polynomials will be described.

## 5.2 Out-of-plane Distortion Induced by Thin Film Stresses

Thin film deposition of metals often results in residual stress [28]. These stresses are characterized into thermal stress and intrinsic stress. Thermal stresses are induced by mismatch of coefficients of thermal expansion between the metal and wafer during the deposition process. Intrinsic stresses are induced by change of atomic packing density, and can be results of gas entrapments, state changes in polymer films, and ion bombardments during doping or physical deposition processes. Residual stresses in thin films will strain the wafer and induce both out-of-plane and in-plane distortions. To simplify the calculations, the wafer will be assumed to be isotropic. The out-of-plane distortion will be axially symmetric under this assumption.

To analyze the effects of thin film residual stresses, a cross-section diagram is

shown in Figure 5-1(a). The wafer has thickness $h$, and the thin film has thickness $t$, where $h \gg t$. Figure 5-1(b) shows the residual stress in the film before the wafer is released, since the wafer is usually constrained during the deposition process. After release the wafer will have some in-plane strain, given by,

$$\epsilon_{in-plane} = \frac{\sigma_o t}{E_{bi,film}t + E_{bi,si}h},$$ (5.1)

where $E_{bi}$ is the biaxial modulus, and $\sigma_o$ is the initial residual stress. The range of the axial strain for typical films is in the order of nanometers, so it will be ignored in further calculation.

After the wafer is released, the residual stress of the film will cause a net moment, resulting in out-of-plane distortions. As the wafer bends, stress gradients develop within the wafer. The bending will stop at static equilibrium, when the sum of the moments about the center of gravity is zero, as shown in Figure 5-1(c). The out-of-plane distortion can be derived from calculating the net moment from the residual stress,

$$M = \int_{-\frac{h}{2}}^{\frac{h}{2}+t} \sigma_o y \, dy.$$ (5.2)

For thin films it can be assumed that the force of the film stress is located at the interface only, which gives,

$$M = \sigma_o \frac{h}{2}t.$$ (5.3)

Substituting into the beam equation for pure bending,

$$\frac{1}{\rho} = \frac{M}{E_{bi}I},$$ (5.4)

where $E_{bi}$ is the biaxial modulus, and $I$ is the second moment of inertia of the wafer. The material and geometric dependencies on the thin film are neglected because $h \gg t$. Substituting,

$$\frac{1}{\rho} = \frac{\sigma_o \frac{h}{2}t}{\frac{E_{bi}}{12}h^3} = \frac{6\sigma_o t}{E_{bi}h^2}.$$ (5.5)

67
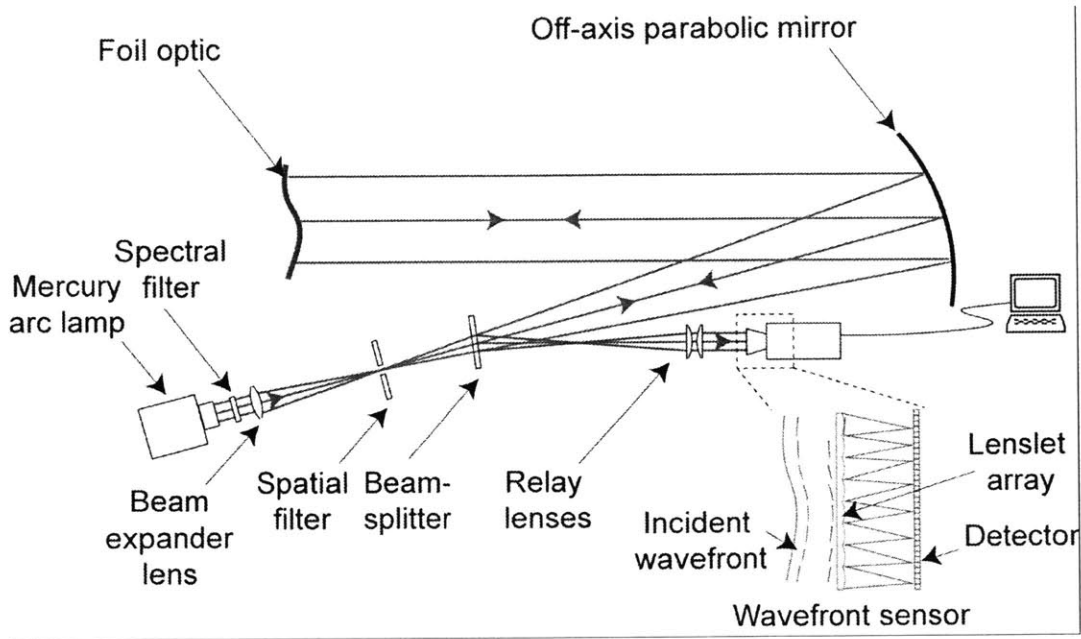
Figure 5-2: The setup for Shack-Hartmann surface metrology tool.

Equation 5.5 is also known as Stoney equation, a useful relationship between the radius of curvature and residual stress for thin films. For wafers with initial curvature, the out-of-plane distortion induced by the residual stress is,

$$\frac{1}{\rho} - \frac{1}{\rho_o} = \frac{6\sigma_o t}{E_{bi}h^2},$$

(5.6)

This relationship holds as long as the strain is in the elastic regime. Using Equation 5.6, the film stress and be calculated if the induced out-of-plane distortion is known.

## 5.3   Shack-Hartmann Surface Metrology Tool

The Shack-Hartmann surface metrology tool is an optical setup capable of mapping surface profiles. For a better understanding of the Zernike polynomials, a general description of the Shack-Hartmann metrology tool will be given. The system setup is depicted in Figure 5-2.

The setup consists of a mercury arc lamp as the light source. The light goes

68

through a spectral filter, and the output wavelength is a spectrum peaking at around 254 nm. The light then is focused onto a pin hole for high frequency spatial filtering, and continues to the off-axis parabolic mirror. The parabolic mirror has its focus at the pin hole, and thus the reflected light turns into a plane wave. The plane wave reflects off the surface of the test optic, and traverses back on its path onto a 64 by 64 microlenslets array. Each lenslet focuses the incident wave to a spot. Based on the movement of these spots relative to a known optical flat, the local slopes of the incident wavefront can be derived as a function of $x$ and $y$. The slopes can be related to the phase of the incident wavefront through the following equation.

$$\nabla \phi(x,y) = \theta_x(x,y) \ \vec{i} + \theta_y(x,y) \ \vec{j} \ . \tag{5.7}$$

The set of local slopes is then least-square fitted to the Zernike polynomials to reconstruct the phase of the incident wavefront. The phase is dependent on the optical path difference, assuming unity air refractive index. The physical shape of the wafer is then half of the optical path difference.

Wavefront reconstruction of discrete data sets raises questions of orthogonality on the discrete data range, and is an elaborate process. Some of the reconstruction schemes are outlined in Malacara [20]. For our experiments a software package written by WavreFront Sciences[2] is used. The algorithm used does not assume orthogonality to simplify computation. For uniform or circularly symmetric irradiance distribution the non-orthogonality is around 1-2% [30].

## 5.4   Zernike Polynomials

The Zernike polynomials are commonly used in describing wavefront functions over a circular pupil [20]. They are defined over a unit circle, such as the one shown in Figure 5-3. The Zernike polynomials play an important role in wavefront representation because they are orthogonal and complete over the unit circle. These polynomials

---

[2]WaveFront Sciences, Inc., 14810 Central Ave SE, Albuquerque, NM 87123, http://www.wavefrontsciences.com
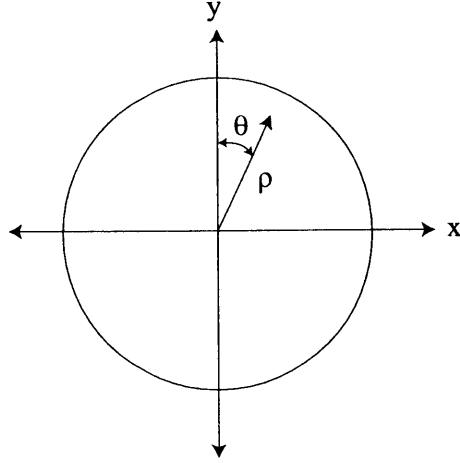
Figure 5-3: Coordinate axis for Zernike polynomials.

can be separated into even and odd functions, given by the following equations. The even function,

$$^eU_n^l(\rho, \theta) = R_n^l(\rho)\cos l\theta, \tag{5.8}$$

and the odd function,

$$^oU_n^l(\rho, \theta) = R_n^l(\rho)\sin l\theta, \tag{5.9}$$

where $n$ is the polynomial order, $l$ is the azimuthal frequency, $\rho$ is the radius, $\theta$ is the angle from vertical, and $R_n^l$ is a radial function. Since the sinusoidal terms are orthogonal[3] over $\theta = 0$ - $2\pi$, the radial function must be orthogonal from $\rho = 0$ - $1$ for $U$ to be orthogonal over the unit circle. The radial function is defined as,

$$R_n^{n-2m}(\rho) = \sum_{s=0}^{m} \frac{(-1)^s(n-s)!}{s!(m-s)!(m-n-s)!}\rho^{n-2s}, \tag{5.10}$$

where $m$ is the mode within a $n$ order. Note that $l$ from Equations 5.8 and 5.9 is defined as $n$-$2m$. The function is odd when $l$ is greater than zero, and even when $l$ is less than zero. When $l$ is zero, the function has no angular dependency, and thus is axially symmetric.

---

[3]Orthogonality of sinusoidal functions are widely known in Fourier series.

(a) Defocus: $2\rho^2 - 1$

(b) Astigmatism: $\rho^2 \cos 2\theta$

(c) Coma: $(3\rho^3 - 2\rho)\cos\theta$

(d) Spherical: $6\rho^4 - 6\rho^2 + 1$
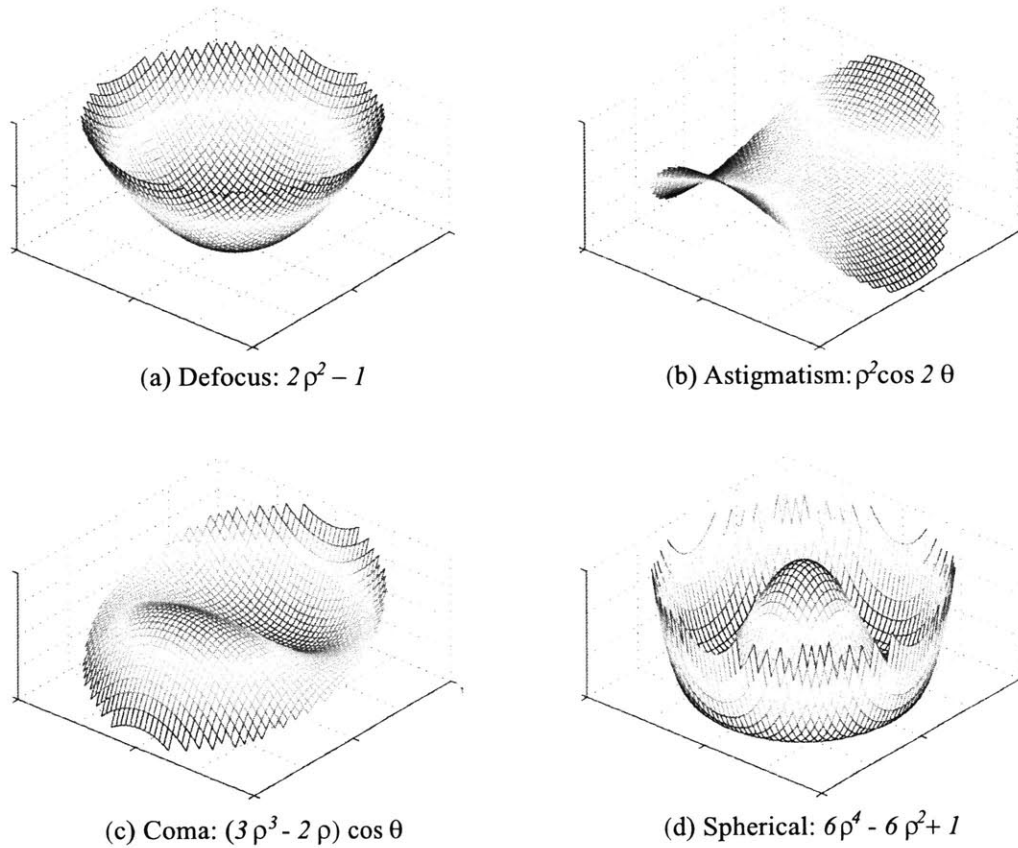
Figure 5-4: Common primary aberrations and their Zernike polynomial functions. (a) Defocus, (b) astigmatism along $y$, (c), coma along $y$, and (d) spherical aberration.

The Zernike polynomials can also describe optical aberration functions. Some commonly known primary aberrations and their Zernike polynomial functions are illustrated in Figure 5-4. They are defocus ($n = 2$, $l = 0$), astigmatism along $y$-axis ($n = 2$, $l = -2$), (c), coma along $y$-axis ($n = 3$, $l = -1$), and (d) spherical aberration ($n = 4$, $l = 0$). For $l = 0$ axially symmetry can be seen, and for $l = -1$ and $l = -2$, axial symmetry and two-fold symmetry are observed, respectively. A more detailed table of Zernike polynomials up to the fifth order is shown in Appendix C.

Since the Zernike polynomials are orthogonal and complete over the unit circle, any wavefront can be described as linear combinations of them. The Zernike co-efficients are the weight factor associated to each polynomial. Since the wavefront function can be described as a linear combination of the Zernike polynomials, the
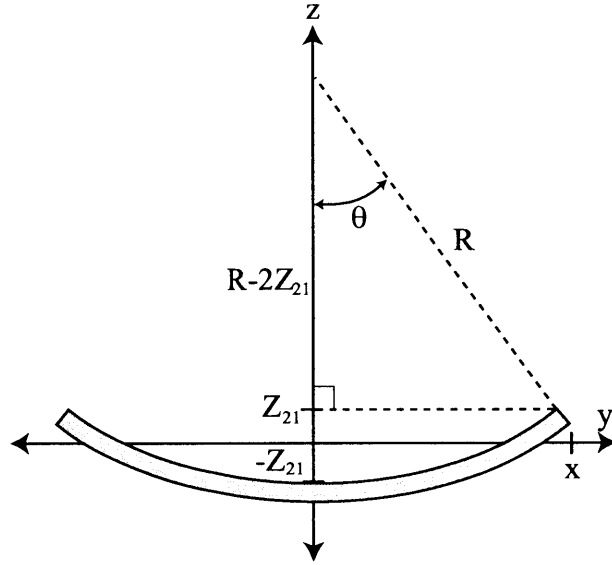
Figure 5-5: $yz$-plane cross-section of a wafer with $Z_{21}$ distortion only.

Zernike coefficients for a given polynomial of two different wavefronts can be compared quantitatively. Thus, if the Zernike polynomials associated with the thin film induced out-of-plane distortion, the associated Zernike coefficients before and after film deposition can be compared directly.

## 5.5 Second Order Zernike Polynomial $Z_{21}$

Based on Equation 5.5, for an isotropic material the curvature induced by residual film stress is axially symmetric. The Zernike polynomials that are axially symmetric have $l = 0$. Disregarding the zeroth order "piston" or constant offset, the next polynomial is $Z_{21}$, given by,

$$Z(\rho) = Z_{21}(2\rho^2 - 1), \tag{5.11}$$

where $Z_{21}$ is the Zernike coefficient. The function is independent of $\theta$, and is thus axially symmetric. A curvature can also be derived based on the weight of the coefficient. Figure 5-5 illustrates a $yz$-plane cross-section of a wafer with a pure $Z_{21}$ distortion,

72

where $Z_c$ is the radius of the wafer. Assuming $\theta$ is small,

$$x = R\sin\theta = R\theta = R_c. \tag{5.12}$$

Simple geometry can calculate the curvature, given by,

$$\frac{1}{R} = \frac{4Z_{21}}{R_c^2 + Z_{21}^2}. \tag{5.13}$$

For small strains, $R_c \gg Z_{21}$, and the higher order term can be omitted, giving,

$$\frac{1}{R} = \frac{4Z_{21}}{R_c^2}. \tag{5.14}$$

In Equation 5.14 the $R_c$ is a geometric constant, and the curvature is linearly related to the magnitude of the Zernike coefficient. In Equation 5.6, aside from the material and geometric constants, the curvature is also linearly related to the residual stress $\sigma_o$. Combining Equation 5.6 and Equation 5.14,

$$\sigma_o = \frac{2E_{bi}h^2}{3tR_c^2}\triangle Z_{21}, \tag{5.15}$$

In Equation 5.15 the residual stress is related to a constant term combining geometric and material properties, and directly proportional to the change in $Z_{21}$. Therefore for small strains, the residual stress and the $Z_{21}$ Zernike coefficients can be related linearly.

## 5.6   Out-of-plane Distortion Experiment

To test the validity of the prediction made in the earlier section relating the residual stress and the $Z_{21}$ coefficients, a thin film deposition experiment was conducted. The back surface profile of a 100 mm silicon (100) wafer was characterized using the Shack-Hartmann tool. 20 nm of Cr was deposited on the front surface by electron-beam evaporation. Cr films were chosen because they are notorious for have high residual film stress.
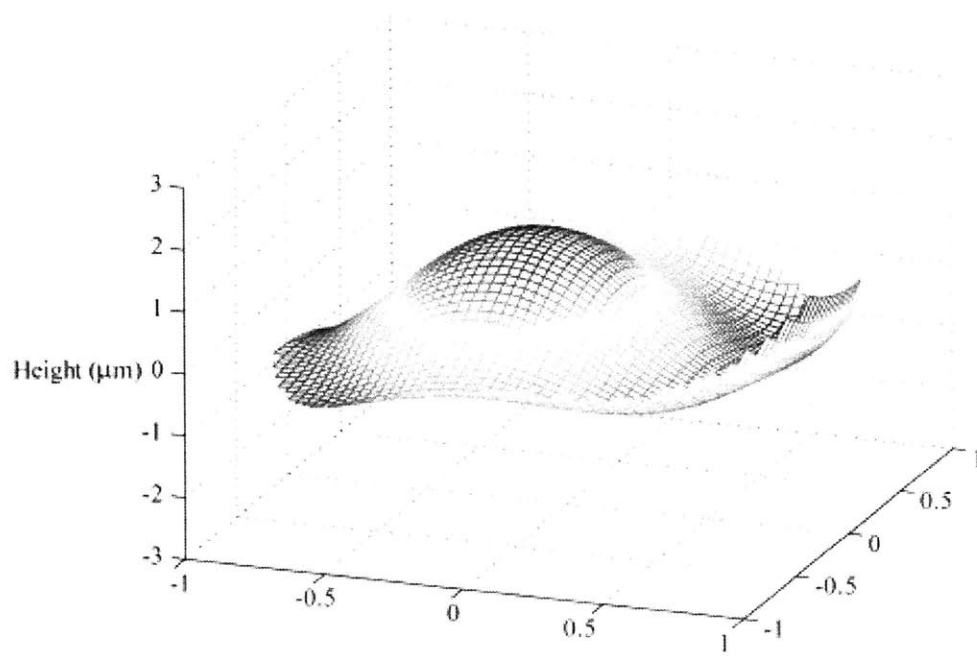
(a)
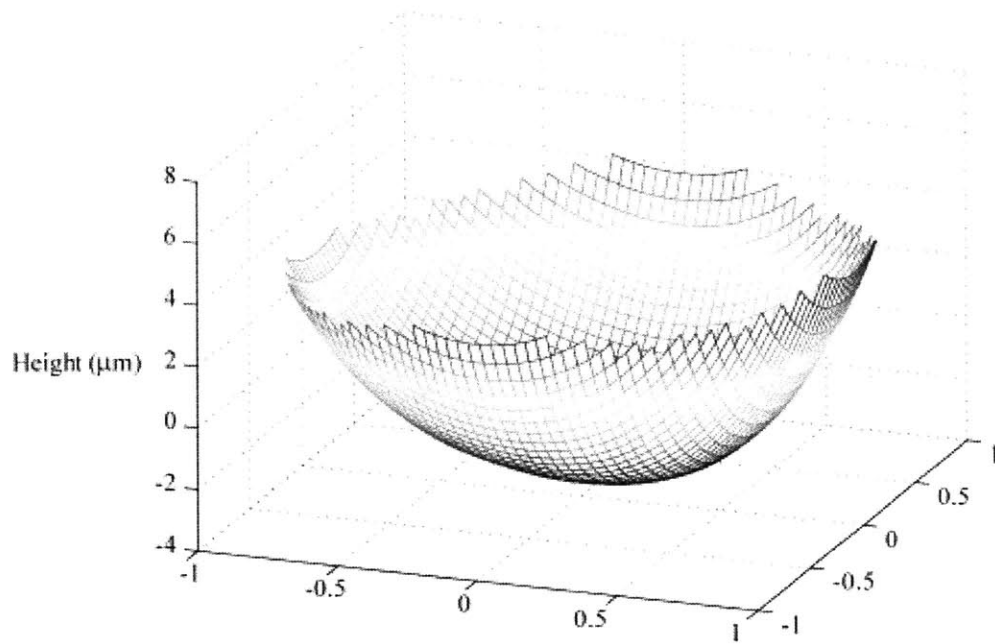


(b)

Figure 5-6: Back surface profile (a) before, and (b) after 20 nm Cr deposition on a normalized x-y scale.

| Term | Pre-Cr Coef (µm) | Post-Cr Coef (µm) | Polar Coord | Description |
|---|---|---|---|---|
| Rz (m) | 3.64E-02 | 3.64E-02 | | |
| Z00 | 0.00E+00 | 0.00E+00 | 1 | piston or constant |
| Z10 | 0.17 | 0.55 | $r\sin\theta$ | tilt about y axis |
| Z11 | -0.462 | -0.153 | $r\cos\theta$ | tilt about z axis |
| Z20 | 0.179 | 0.069 | $r^2\sin2\theta$ | astigmatism with axis +/- 45 |
| Z21 | -0.574 | 3.518 | $2r^2-1$ | focus shift |
| Z22 | 0.228 | 0.231 | $r^2\cos2\theta$ | astigmatism with 0 or 90 axis |
| Z30 | 0.226 | 0.176 | $r^3\sin3\theta$ | triangular astigmatism with base on x-axis |
| Z31 | -0.815 | -0.617 | $(3r^3-2r)\sin\theta$ | third order coma along x-axis |
| Z32 | -0.09 | -0.037 | $(3r^3-2r)\cos\theta$ | third order coma along y-axis |
| Z33 | 0.219 | 0.185 | $r^3\cos3\theta$ | triangular astigmatism with base along y-axis |
| Z40 | 0.05 | 0.027 | $r^4\sin4\theta$ | |
| Z41 | -0.03 | -0.054 | $(4r^4-3r^2)\sin2\theta$ | |
| Z42 | 0.552 | 0.538 | $6r^4-6r^2+1$ | third order spherical aberration |
| Z43 | -0.157 | -0.16 | $(4r^4-3r^2)\cos2\theta$ | |
| Z44 | 0.391 | 0.374 | $r^4\cos4\theta$ | |

Figure 5-7: Table of the Zernike polynomials before and after Cr deposition.

During the data acquisition process the spot focused by the lenselet array shifts rapidly due to environmental issues such as air turbulence and thermal gradients. The high frequency jittering effect is reduced by averaging over 100 samples. The reconstruction algorithm automatically defines the Zernike circle at the center of the wafer, and least-square fits up to the fifth order Zernike polynomials.

The back surface profile before Cr deposition is shown in Figure 5-6(a), and has a peak-valley (P-V) value of 2.43 $\mu$m. The back surface profile after Cr deposition is shown in Figure 5-6(b). The wafer is distorted in the opposite direction, and has a P-V of -8.93 $\mu$m. Since the wafer has an initial warp that is random, direct height comparison of the two surface maps is tedious. In order to simply take the difference the maps must lie on the same spatial coordinate with the same orientation. However, if we examine the Zernike coefficients before and after the Cr deposition, as shown in Figure 5-7, more insight about the out-of-plane distortion can be realized.

In Figure 5-7 the first column is the Zernike coefficient order, the second and third columns are the coefficient values before and after Cr deposition, respectively. The $Z_{10}$ and $Z_{11}$ coefficients corresponds to the average tilt, which is related to the physical
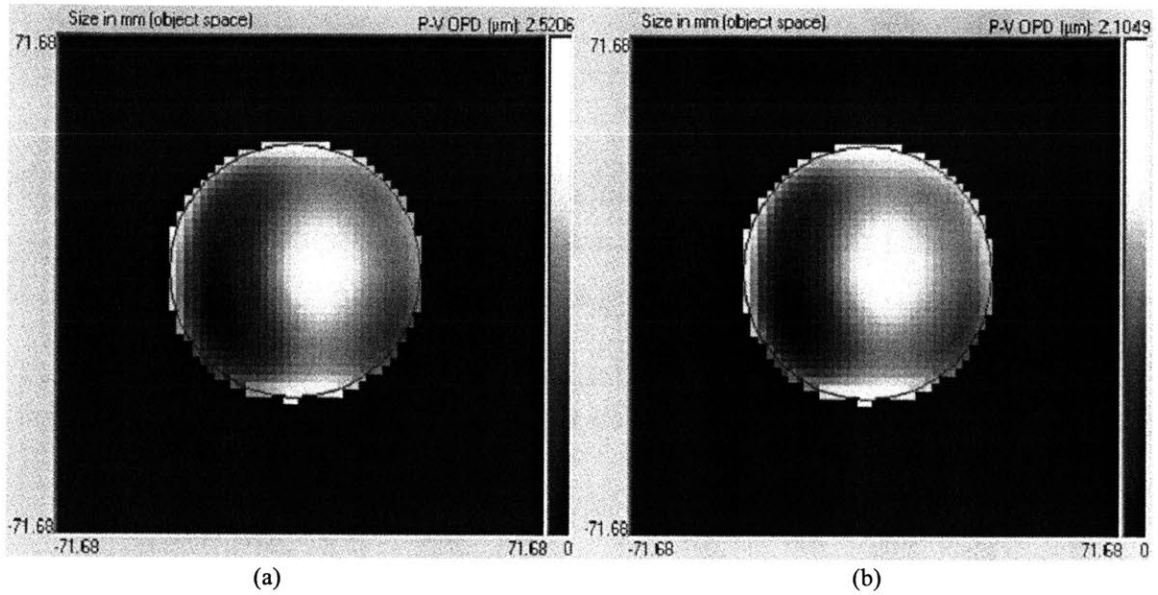
Figure 5-8: Measured surface profile after subtracting the $Z_{21}$ polynomial for (a) before, and (b) after Cr deposition.

mount position of the wafer. The tilt coefficients are taken out of the comparison. From Figure 5-7 the change in the $Z_{21}$ coefficient is $\sim$4 $\mu$m, compared to $\sim$0.1 $\mu$m for the next highest difference. Since the dynamic repeatability of the Shack-Hartmann system is in the range of 0.1 $\mu$m, the changes in the other coefficients are not physical. Therefore, the strong direct dependency of the out-of-plane distortion to the $Z_{21}$ coefficient only can be observed.

Since the fitted Zernike polynomial functions are almost perfectly orthogonal, individual coefficients can be taken out without affecting the other orders. To further confirm the dependency of the film induced distortion, the $Z_{21}$ polynomial is taken out from both wafer surface profiles before and after Cr deposition, as shown in Figure 5-8. The resulting profiles look almost identical. The physical shapes of the two surface profiles are radically different. Yet taking away the effect of the $Z_{21}$ related out-of-plane distortion, the wafers surface resemble each other closely.

In this experiment it can be seen that film induced out-of-plane distortions are related only to the $Z_{21}$ polynomial. Thus using Equation 5.15, the film stress can be directly calculated to be,

76

$$\sigma_o = \frac{2(130 \ Gpa)(500 \ \mu m)^2}{3(1 - 0.266)(20 \ nm)(3.64 \ mm)^2}(-\frac{4.092}{2}) \ \mu m = -2.98 \ Gpa, \qquad (5.16)$$

## 5.7 Anisotropic Materials

Much of the analysis done is based on a wafer with isotropic material, which has only two independent terms in the compliance matrix. Silicon is a cubic material with three independent compliance terms, thus the real out-of-plane distortion would be expected to be more complex. [4] presents a detailed analysis on such anisotropic materials. The generalized Hooke's Law involves a forth order compliance tensor for a cubic material is shown as,

$$
\begin{bmatrix} \epsilon_1 \\ \epsilon_2 \\ \epsilon_3 \\ \epsilon_4 \\ \epsilon_5 \\ \epsilon_6 \end{bmatrix} = \begin{bmatrix} S_{11} & S_{12} & S_{12} & 0 & 0 & 0 \\ S_{12} & S_{11} & S_{12} & 0 & 0 & 0 \\ S_{12} & S_{12} & S_{11} & 0 & 0 & 0 \\ 0 & 0 & 0 & S_{44} & 0 & 0 \\ 0 & 0 & 0 & 0 & S_{44} & 0 \\ 0 & 0 & 0 & 0 & 0 & S_{44} \end{bmatrix} \begin{bmatrix} \sigma_1 \\ \sigma_2 \\ \sigma_3 \\ \sigma_4 \\ \sigma_5 \\ \sigma_6 \end{bmatrix}, \qquad (5.17)
$$

where $\epsilon_i$ and $\sigma_i$ are the second order strain and stress tensors, respectively. To calculate an effective Young's modulus for any given crystal lattice, tensor transformation will be used. Given an arbitrary Miller indices direction $[h,k,l]$, the coordinate reference can be defined as shown on Figure 5-9. The compliance stiffness [14] given by Equation 5.17 will be transformed to the new axis by,

$$S'_{mnpq} = l_{im}l_{jn}l_{kp}l_{lq}S_{ijkl}, \qquad (5.18)$$

where $S'_{mnpq}$ and $S_{ijkl}$ are the compliance matrix associated with the arbitrary axis and the reference axis, respectively. The $l$ are the direction cosines between the reference coordinate and the arbitrary direction. The effective modulus along the transformed x-axis will then be,
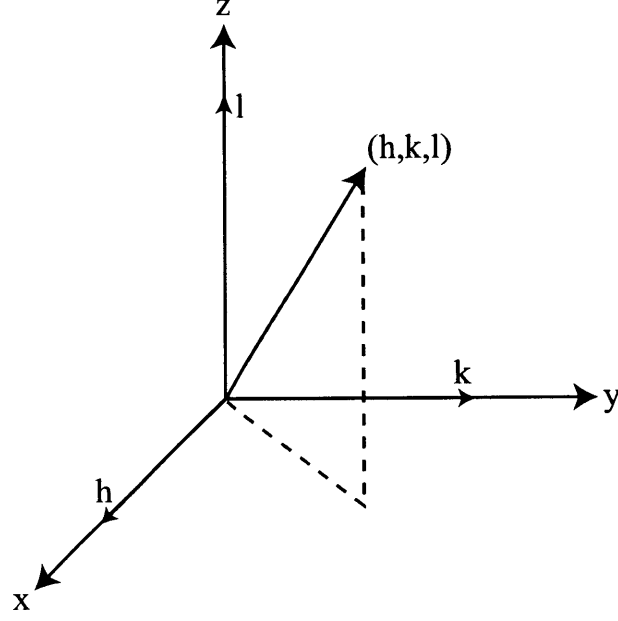
Figure 5-9: Reference coordinate system for an arbitrary direction.

$$E' = \frac{1}{S'_{1111}} = \frac{1}{S'_{11}} = \frac{1}{S_{11} - (2S_{11} - 2S_{12} - S_{44})(l_1^2 l_2^2 + l_2^2 l_3^2 + l_1^2 l_3^2)}, \qquad (5.19)$$

where $l_1$, $l_2$, and $l_3$ are direction cosines between $[h,k,l]$ and the reference x-axis, and are given by,

$$(l_1, l_2, l_3) = \left(\frac{h}{\sqrt{h^2 + k^2 + l^2}}, \frac{k}{\sqrt{h^2 + k^2 + l^2}}, \frac{l}{\sqrt{h^2 + k^2 + l^2}}\right). \qquad (5.20)$$

Using the transformed compliance tensor, the effective Poisson's ratio is,

$$\nu'_{12} = -\frac{S'_{12}}{S'_{11}} = -\frac{S_{12} + \frac{1}{2}(2S_{11} - 2S_{12} - S_{44})(l_1^2 m_1^2 + l_2^2 m_2^2 + l_3^2 m_3^2)}{S_{11} - (2S_{11} - 2S_{12} - S_{44})(l_1^2 l_2^2 + l_2^2 l_3^2 + l_1^2 l_3^2)}, \qquad (5.21)$$

where $m_1$, $m_2$, and $m_3$ are the direction cosines between the shear direction and the reference x-axis. Using Equations 5.19 and 5.21, the effects of the anisotropic material property can be predicted in different orientation silicon wafers. Three commercially available silicon orientation wafers, the (100), (110), and the (111) will be analyzed.

78
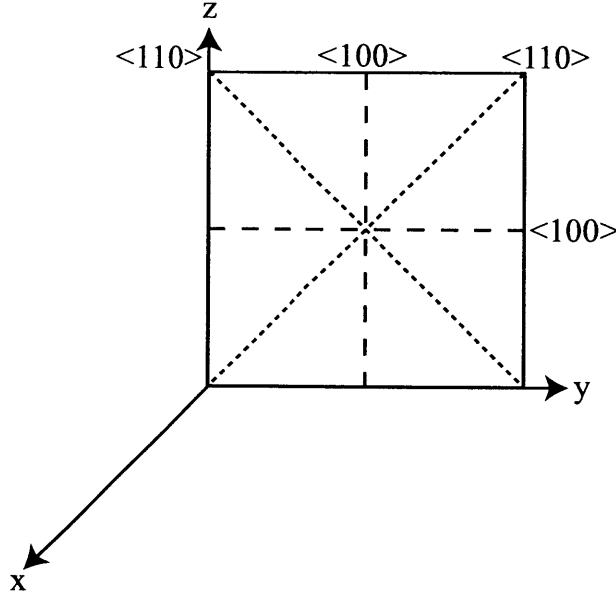
Figure 5-10: Crystal orientation for a (100) silicon.

## 5.7.1  (100) Orientation Silicon

(100) Silicon has the [100] direction as the wafer normal, as shown in Figure 5-10. Thus for all the directions $[h,k,l]$ that can lie on the (100) plane,

$$[1, 0, 0] \cdot [h, k, l] = 0. \tag{5.22}$$

The $m_i$ can also be defined as,

$$[m_1, m_2, m_3] = [1, 0, 0] \times [h, k, l]. \tag{5.23}$$

From these two relationships, Equation 5.19 and 5.21 for (100) orientation silicon can be simplified to,

$$E'_{(100)} = \frac{1}{S_{11} - (2S_{11} - 2S_{12} - S_{44})l_2^2 l_3^2}, \tag{5.24}$$

and,

$$\nu'_{(100)} = -\frac{S_{12} - (2S_{11} - 2S_{12} - S_{44})(l_2 l_3 m_2 m_3)}{S_{11} - (2S_{11} - 2S_{12} - S_{44})l_2^2 l_3^2}. \tag{5.25}$$

| 1 | [001] | [011] |
|---|---|---|
| m | $[0\bar{1}0]$ | $[0\bar{1}1]$ |
| $E'$ (Gpa) | 130.2 | 168.9 |
| $\nu'$ | 0.279 | 0.0642 |
| $E'_{bi}$ (Gpa) | 180.5 | 180.5 |

Table 5.1: Modulus and Poisson's ratio in a (100) silicon.

From Equations 5.24 and 5.25 it can be seen that both the Young's modulus and Poisson's ratio are dependent on the direction vectors. However, these relationships are for 1-dimensional approximations. For a case with 2-dimensional wafer, the effect of shear in the perpendicular direction needs to be accounted for, and the biaxial modulus is used. The biaxial modulus is given by,

$$E_{bi} = \frac{E}{1 - \nu}. \tag{5.26}$$

Substituting Equation 5.24 and 5.25 yields,

$$E'_{bi,(100)} = \frac{E'_{(100)}}{1 - \nu'_{(100)}} = \frac{1}{S_{11} + S_{12}}. \tag{5.27}$$

From Equation 5.27 it can be seen that the biaxial modulus is independent of directions on the (100) plane. This result can be explained both physically and mathematically. Figure 5-10 shows that for any arbitrary direction on the (100) plane, the shear direction would be of the same family. This is the result of the cubic material property, in which a $90^\circ$ rotation along the [100] axis would result in an identical crystal. Thus the $l_i$ and $m_i$ direction cosines, for any given direction $[h,k,l]$, would belong to the same Miller indices family, and therefore have the same property. Mathematically, $[0, m_2, m_3] = [0, -l_3, l_2]$ for all directions in the (100) plane, and thus cancels out in deriving Equation 5.27. Therefore for a (100) silicon there will be no directional dependency on thin film induced out-of-plane distortions. Table 5.1 shows some calculated values along different directions in a (100) orientation silicon.

| l | $[01\bar{1}]$ |
|---|---|
| m | $[\bar{2}11]$ |
| E' (Gpa) | 168.9 |
| $\nu'$ | 0.262 |
| $E'_{bi}$ (Gpa) | 229.0 |

Table 5.2: Invariant modulus and Poisson's ratio in a (111) silicon.

## 5.7.2  (111) Orientation Silicon

For (111) silicon, the directional cosines $l_i$ and $m_i$ can be greatly simplified. For all directions in the (111) plane,

$$[1, 1, 1] \cdot [h, k, l] = 0, \tag{5.28}$$

and the direction cosine relationship,

$$l_1^2 + l_2^2 + l_3^2 = 1. \tag{5.29}$$

Solving these equations will yield $l_1^2 l_2^2 + l_2^2 l_3^2 + l_1^2 l_3^2 = \frac{1}{4}$ and $l_1^2 m_1^2 + l_2^2 m_2^2 + l_3^2 m_3^2 = \frac{1}{6}$. Thus the directional dependency factors for both the modulus and Poisson's ratio are invariant in a (111) plane. The modulus is given by,

$$E'_{(111)} = \frac{4}{2S_{11} + 2S_{12} + S_{44}}, \tag{5.30}$$

and the Poisson's ratio given by,

$$\nu'_{111} = -\frac{S_{11} + 5S_{12} - \frac{1}{2}S_{44}}{3(S_{11} + S_{12} + \frac{1}{2}S_{44})}. \tag{5.31}$$

The biaxial modulus is then,

$$E'_{bi,(111)} = \frac{6}{4S_{11} + 8S_{12} + S_{44}}. \tag{5.32}$$

Table 5.2 shows the calculated invariant modulus in a (111) orientation silicon.
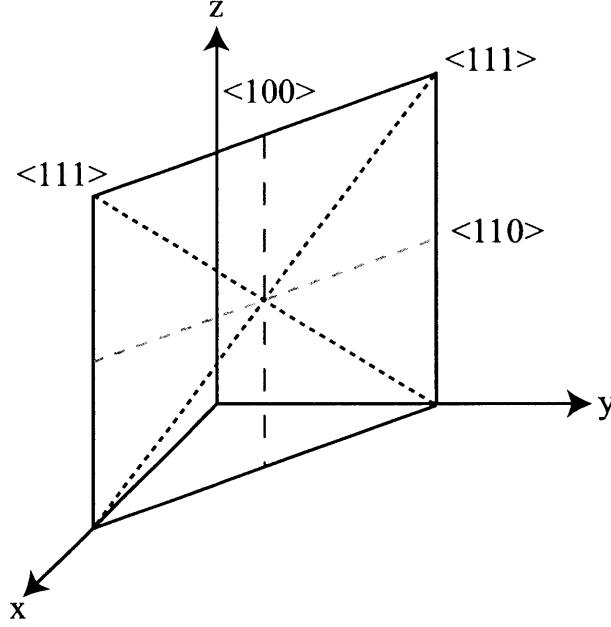
Figure 5-11: Crystal orientation for a (110) silicon.

## 5.7.3 (110) Orientation Silicon

(110) orientation silicon, as shown on Figure 5-11, has the most complicated directional dependency. For (110) silicon any given direction on the surface will satisfy,

$$[1, 1, 0] \cdot [h, k, l] = 0, \tag{5.33}$$

and Equation 5.29. Using these two equations the modulus of any given direction in a (110) plane can be simplified as,

$$E'_{(110)} = \frac{1}{S_{11} - (2S_{11} - 2S_{12} - S_{44})l_1^2(2 - 3l_1^2)}, \tag{5.34}$$

and,

$$\nu'_{(110)} = -\frac{S_{12} + \frac{1}{2}(2S_{11} - 2S_{12} - S_{44})(6l_1^2 m_1^2 - 2l_1^2 - 2m_1^2 + 1)}{S_{11} - (2S_{11} - 2S_{12} - S_{44})l_1^2(2 - 3l_1^2)}. \tag{5.35}$$

Combining Equation 5.34 and 5.35 yields,

82

| l | [001] | [1$\bar{1}$1] | [1$\bar{1}$0] |
|---|---|---|---|
| m | [1$\bar{1}$0] | [1$\bar{1}$2] | [00$\bar{2}$] |
| E$'$ (Gpa) | 130.2 | 187.5 | 168.9 |
| $\nu'$ | 0.279 | 0.181 | 1.3615 |
| E$'_{bi}$ (Gpa) | 180.5 | 229.0 | 264.6 |

Table 5.3: Modulus and Poisson's ratio in a (110) silicon.

$$E'_{bi,(110)} = \frac{1}{S_{11} + S_{12} + \frac{1}{2}(2S_{11} - 2S_{12} - S_{44})(6l_1^4 + 6l_1^2 m_1^2 - 6l_1^2 - 2m_1^2 + 1)}. \quad (5.36)$$

From Equation 5.36 the direction dependency factors, $l_1$ and $m_1$, are still present. These results are due to the fact that for a given direction in a (110) plane, the $l_i$ and $m_i$ do not belong to the same family directions. Figure 5-11 depicts this point. A rotation about the [110] direction would not yield an identical crystal. Thus the $l_1$ and $m_1$ direction cosines are independent of each other, and thus both contribute to the biaxial modulus. Table 5.3 shows some calculated values along different directions for a (100) silicon.

The lattice dependency of biaxial stiffness modulus in (110) orientation silicon can be observed. However the question of whether these asymmetrical distortions can be broken down into linear combinations of Zernike polynomials remain unanswered. Initial prediction will focus on the $Z_{40}$, $Z_{44}$, $Z_{20}$, and $Z_{22}$ Zernike polynomials. Experiments with (110) silicon are needed to be performed to test the validity of the theory.

## 5.8 Conclusion

In the theoretical model and experimental results, the out-of-plane distortion induced by thin film residual stress is found to be solely dependent on the $Z_{21}$ Zernike polynomial for small strains. Instead of subtracting the height profile of the surface maps, the $Z_{21}$ Zernike coefficients can be directly compared to give a more quantitative

analysis of the out-of-plane distortion. The residual stress of the deposited film is also derived to be a linearly dependent on the difference of the $Z_{21}$ coefficients. More experiments will be conducted to test the lattice dependency distortion on (110) orientation silicon.

# Chapter 6

# X-ray Diffraction Testing

## 6.1  Introduction

The surface qualities of both the anisotropically etched silicon grating and replicated polymer grating are encouraging. The blazed facets are extremely smooth, with roughness in the order of 0.15 nm. However these physical data do not guarantee high optical performance. Both type of gratings were tested for x-ray diffraction efficiencies, and the results will be outlined in this chapter. The gratings have been tested in a number of x-ray source facilities, including point sources and synchrotron radiation beamlines. The results that will be reported were conducted at the Center for X-ray Optics of Lawrence Berkeley National Laboratory and the National Synchrotron Light Source of Brookhaven National Laboratory.

## 6.2  X-ray Diffraction Testing

The anisotropically-etched silicon and NIL replicated polymer gratings were tested in an off-plane configuration, where the incident x-rays are parallel to the grating lines. The diffracted orders are then diffracted into a half cone. Detailed specifications of the testing geometry are outside the scope of this thesis. Some of the results have different testing geometries so the peaks might be shifted. At this phase of research the most important factor is the comparison of the maximum diffracted intensities of

Figure 6-1: (a) Diffraction efficiencies of diffracted orders, and (b) conic diffraction pattern for a silicon blazed grating in the off-plane mount.

the silicon and polymer grating.

The x-ray diffraction efficiency of the anisotropically etched silicon grating is shown in Figure 6-1. The diffraction efficiencies are plotted against wavelength. Figure 6-1(a) illustrates the efficiencies of the different diffracted orders. The maximum efficiency is estimated to be $\sim$0.34 at $\lambda \sim$ 4.5 nm. Figure 6-1(b) depicts the conical diffraction pattern. The diffracted orders are as labeled.

The x-ray diffraction efficiency of an imprinted polymer grating is shown in Figure 6-2. Figure 6-2(a) illustrates the efficiencies of the different diffracted orders. The maximum efficiency is estimated to be $\sim$0.32 at $\lambda \sim$ 2.6 nm. Figure 6-2(b) also depicts the conical diffraction pattern. The diffracted orders are as labeled. The gratings used are the first generation replicas that were imprinted using a manual setup. Several factors, such as release angles, residual thickness, and thickness variations were not well controlled. The minor streaking observed in Figure 6-2(b) might be caused by rounding of the blazed facets.

From these two x-ray diffraction efficiency curves the quality of the imprinted polymer and silicon gratings can be concluded to be in similar magnitude. The
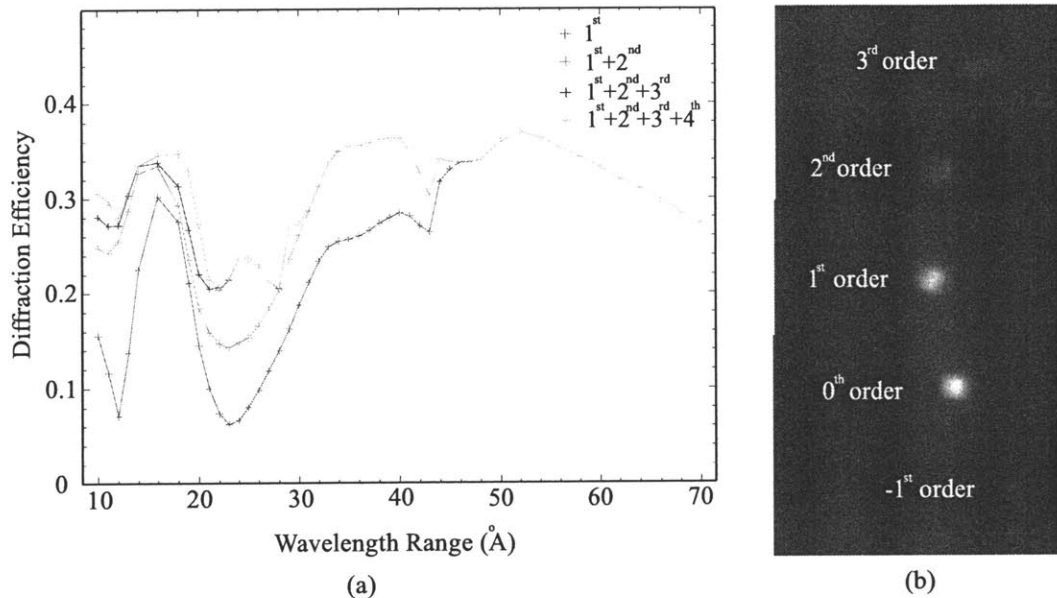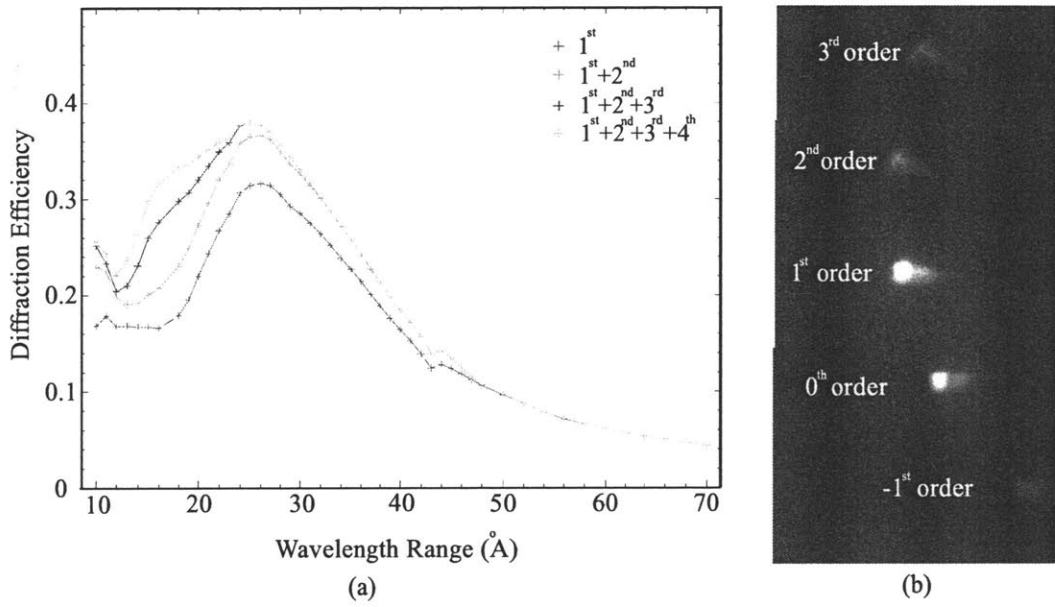
Figure 6-2: (a) Diffraction efficiencies of diffracted orders, and (b) conic diffraction pattern for an imprinted polymer grating in the off-plane mount.

two gratings were tested at different geometries, so the location of the maximum efficiencies can not be directly compared. However these results do show that the imprinted polymer grating does not perform any worse than the silicon master. These data were taken at the Center for X-ray Optics [25].

More recent x-ray diffraction tests have been conducted on a polymer grating imprinted by Nanonex Corporation, as shown in Figure 4-9. One important factor to notice is that the more compliant polymer grating is strained after the metal coating process. An atomic force micrograph depicts the 3-dimensional surface profile of the strained polymer gratings after depositing 5 nm of Ti and 20 nm of Au, in Figure 6-3. The roughened profile can be due to two reasons. The first is the residual stress of the metal films straining the polymer. The stiffness of polymer is in the order of ~1 Gpa, while the residual stress can be up to hundreds of MPa. The second might be local out-gasing of the polymer during the metal deposition process. The metals are thermally evaporated by e-beams, in which when the materials are depositing the temperature might be near the glass transition temperature, resulting in out-gassing.

The conical diffraction pattern of the imprinted polymer blazed grating in an
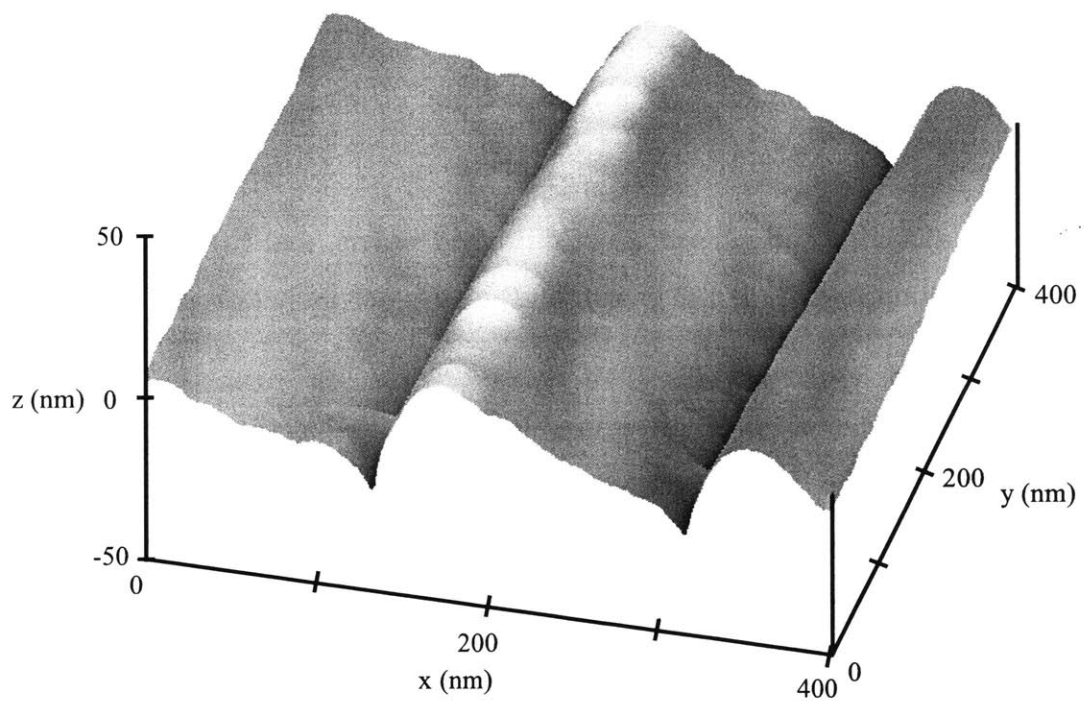
Figure 6-3: AFM 3-dimensional surface profile of a strained imprinted polymer grating.
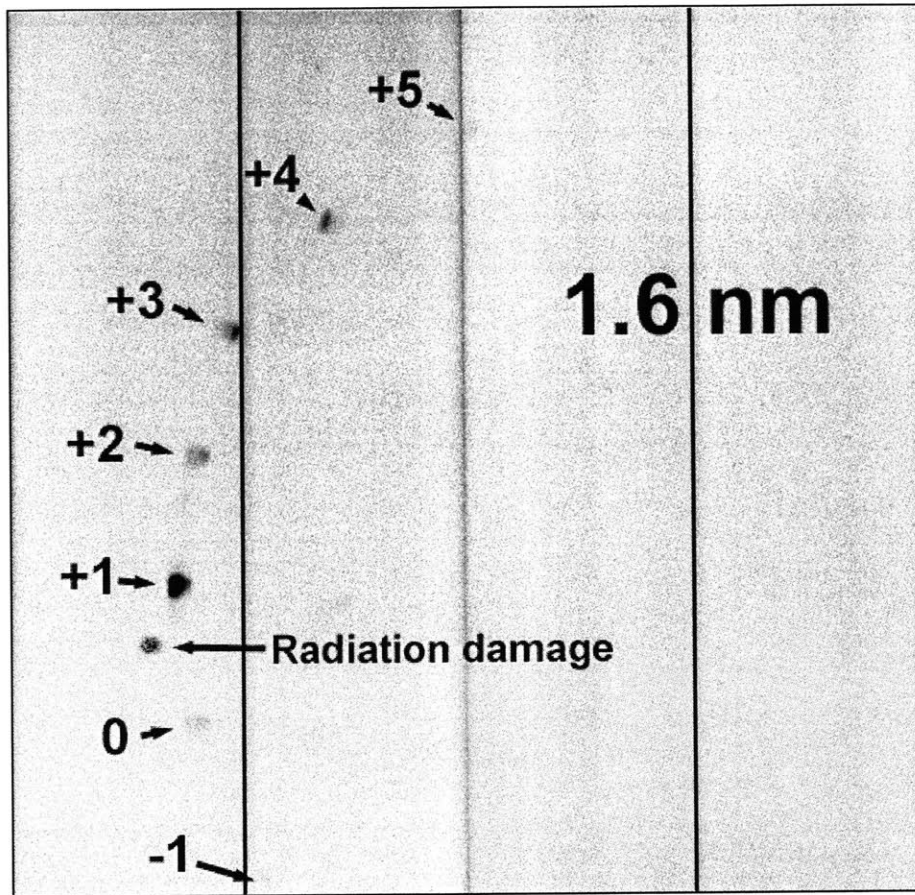
Figure 6-4: Conical diffraction pattern for an off-plane grazing incidence blazed grating.

extreme off-plane mount captured by a CMOS camera is shown in Figure 6-4. The x-ray wavelength is 1.6 nm, and diffraction up to the $5^{th}$ order is strong enough to be detected. The maximum diffracted intensity is shifted to the $+1^{st}$ order due to the effect of the blazed facets.

X-ray diffraction efficiency results were simulated using a commercial software PCGrate. The algorithm involved in the simulation is outlined in [15]. The cross-section of the metal-coated polymer grating, as scanned by the AFM, is used in the simulation. The experimental efficiencies of the first and zeroth orders are plotted with the simulated results in Figure 6-5.

In Figure 6-5, the experimental data agree well to the simulated data. The spikes
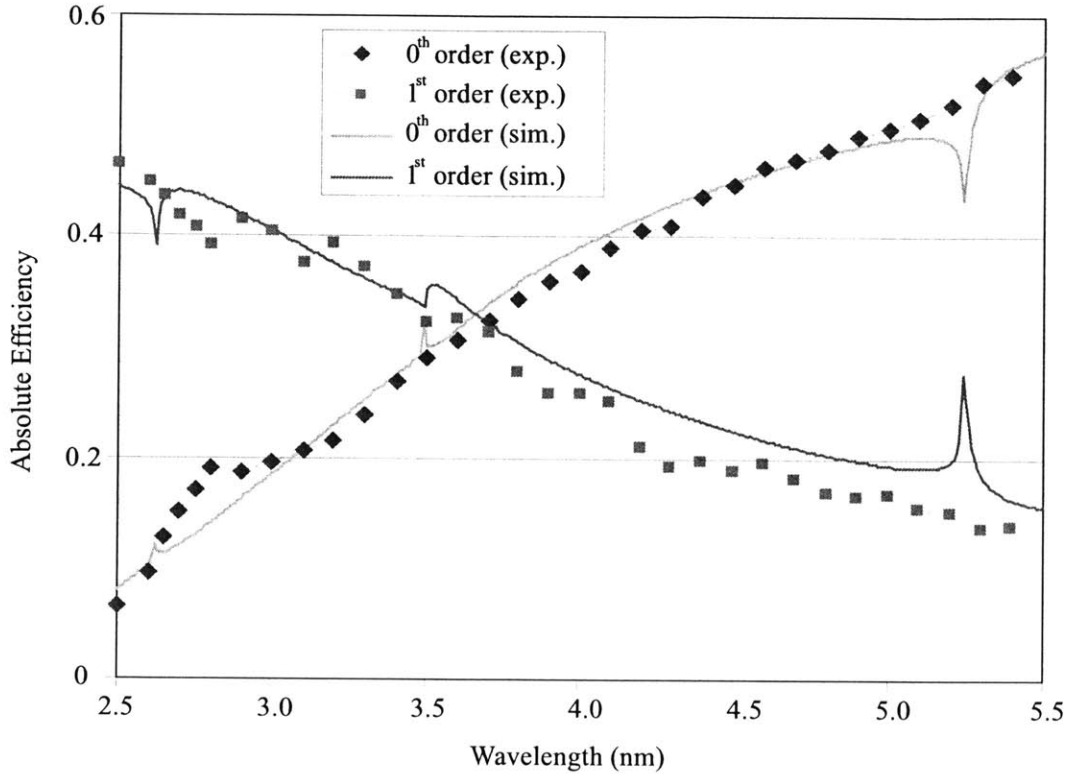
Figure 6-5: Experimental and simulated efficiencies of the first and zeroth order efficiencies.

in the simulated data are not seen in testing. Spikes occur when a higher diffracted order moves out of the physical geometry of the grating and becomes evanescent. In these preliminary results the spikes might be just artifacts of the calculation algorithm. The interpretation of these results are still in progress, yet the high first-order diffracted efficiency at ~0.47 is very encouraging. These x-ray diffraction testings were conducted at the National Synchrotron Light Source of Brookhaven National Laboratory.

## 6.3 Conclusion

From the x-ray diffraction efficiency testing results, it can be seen that the imprinted polymer gratings do not perform worse than the anisotropically etched silicon gratings. The maximum efficiencies of the two gratings are found to be of similar mag-

nitude. Further testing demonstrated that the performance of the imprinted grating agrees closely to the simulated results. It can be concluded that replicating silicon blazed gratings with NIL is a time and cost efficient process, while at the same time not compromising performance.

Future goals include different metal coating materials and processes to reduce strain in the profile. It has been suggested that a curved facet might perform better than a perfectly blazed facets, since these gratings are not designed for a single wavelength. However it is important that the strain of the polymer gratings can be controlled. The mechanical integrity of the polymer grating is also an issue, and different polymer material with higher stiffness will be explored. Furthermore, in-plane distortion during both the NIL and metal deposition processes will be examined.

# Appendix A

# Recipe for 200 nm-period Inverted Triangular and Blazed Gratings

The fabrication recipe for the inverted triangular and $7^o$ blazed gratings are the same, except different orientation wafers are used. For inverted triangular gratings, (100) wafers are used. For the $7^o$ blazed gratings, wafers with its normal rotated $7^o$ from the [111] direction along the [1$\bar{1}$0] axis are used.

1. In ICL, deposit silicon nitride layer.

   - Thickness = 30 nm.

   - Use chemical vapor depostion.

   - VTR tube.

2. In NSL, spincoat Brewer Science ARC-i-con-7.

   - Thickness = 49 nm.

   - Spin speed = 4.9 kRPM.

   - Soft bake on hot plate at 185$^o$C for 1 min.

3. In NSL, spincoat Sumitomo PFI-34a2 photoresist.

   - Thickness = 200 nm.

- Spin speed = 3.75 kRPM.

- Soft bake on hot plate at 95°C for 1 min.

4. In SNL, pattern grating line with interference lithography.

- Half angle = 61.37° for 200 nm-period.

- Dose = 24.8 mJ/cm² for line-space ratio of 1.

- Develop exposed resist in OPD 262 developer for 1 minute.

5. In SNL, RIE ARC layer.

- Chamber 1

- $O_2$ at 45 sccm.

- Pressure = 1.4 mTorr.

- Power = 25 W.

- Etch time = 4.5 minutes.

6. In SNL, RIE silicon nitride layer.

- Chamber 2

- $CHF_3$ at 10 sccm.

- Pressure = 20 mTorr.

- Power = 100 W.

- Etch time = 3 minutes.

7. In SNL, RCA clean.

- $H_2O : H_2O_2 : NH_4 = 5 : 1 : 1$.

- Temperature = 85°C.

- Clean time = 20 min.

8. In NSL, KOH anisotropic etch.

- Solution = 20% KOH by weight.

- Etch temperature = $25^o$C.

- Dip in buffered HF for 15 sec before KOH solution.

- Etch time = 3 min, longer to undercut.

- Check line width in SEM using high acceleration voltage ~10kV.

- During etching the etched profile will appear darker since the surface has lower reflectivity compared to a flat surface.

9. In NSL, etch silicon nitride mask.

- Solution = concentrated HF.

- Etch time ~3 min.

- Wafer surface will turn hydrophobic when all the nitride is etched away.

# Appendix B

# Atomic Force Microscope Noise Analysis

The resolution of an Atomic Force Microscope (AFM) is usually limited by the noise of the system. When scanning smooth surfaces with roughness in the order of $\sim$0.1 nm, the signal level approaches the noise level and the data is hard to interpret. In order to perform accurate measurements on the etched (111) plane for the anisotropically etched gratings, the noise of the AFM used will be analyzed.

## B.1   AFM Noise Level

The noise level of the AFM can be directly characterized by choosing a scan area of zero. In this setting the AFM tip is sampling the same spatial point repeatedly in time. The signal that was a function of time and space is now only a function of time. Ideally, scanning the same point would obtain constant height, and thus all the data will be due to noise. A time domain data of such scan is shown in Figure B-1(a), and its power spectrum is shown in Figure B-1(b). The time domain data is sampled at 128 Hz. Note that only environmental noise will be captured. Noise from other sources during scanning such as the piezoelectric tube can not be sampled with this method.

The power spectrum shows that standard deviation is $\sim$0.118 nm, and the stan-
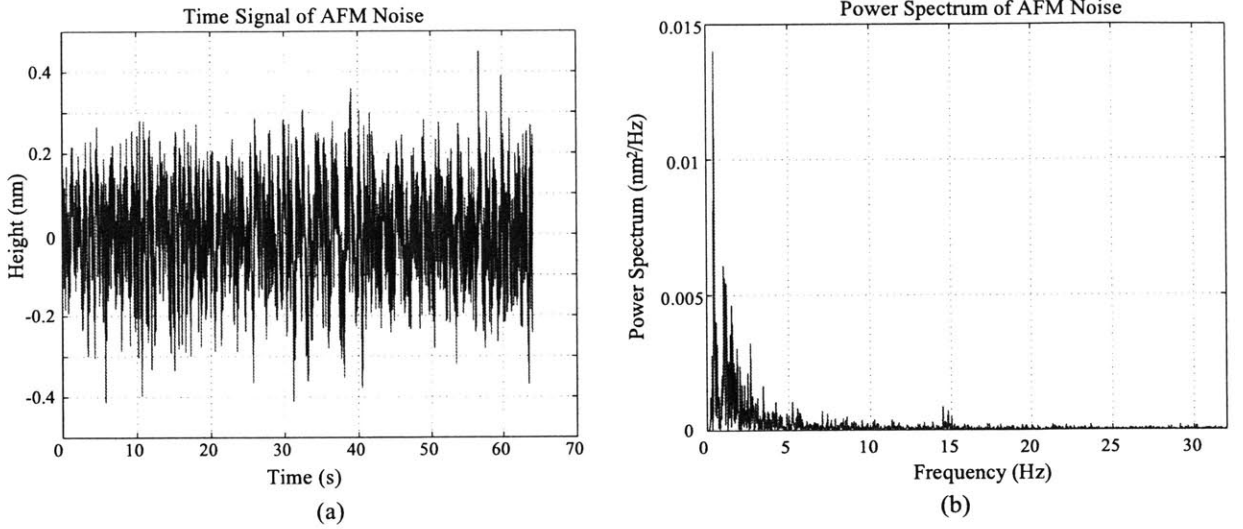
Figure B-1: (a) Time domain, and (b) frequency domain of AFM data for sampling same spatial point.

dard deviation below 5 Hz is ~0.098 nm. Thus most of the noise is due to frequencies less than 5 Hz. Noise can be characterized into vibrational (less than 100 Hz), acoustical (100–1000 Hz), and electrical (60 Hz). Vibrational noise will be analyzed with more detail, since it is believed to be the most significant noise source.

## B.2   Vibration Isolation Stage Performance

The effects of ground vibration are greatly reduced by a vibration isolation stage. The isolation performance of the stage is described by its transmissibility, which is the transfer function of the stage. Passive air isolation stages (the type used for the AFM at MIT's NanoStructures Lab), can be modeled as a second order system. Following the schematic illustrated in Figure B-2, balance of force on the stage yields,

$$M \, \ddot{x}_s \, (t) = k(x_v(t) - x_s(t)) + b \, (\dot{x}_v \, (t) - \dot{x}_s \, (t)) \tag{B.1}$$

where $M$ is the mass of the stage, $k$ is the system stiffness, $b$ is the system damping factor, $x_s(t)$ is the translation of the stage, and $x_v(t)$ is the ground vibration. After Laplace transformation and reorganizing, the transfer function of the isolation stage

Figure B-2: Second order approximation for the vibration isolation stage.

is given by,

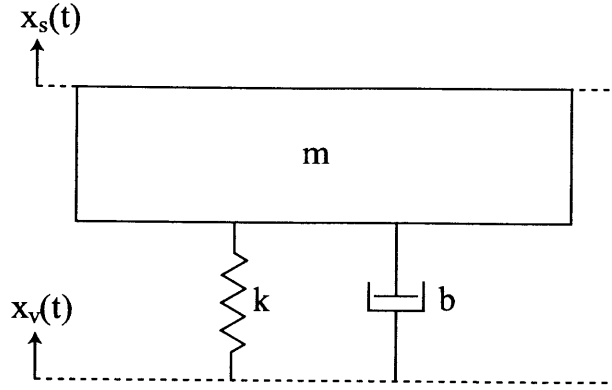$$\frac{X_s(s)}{X_v(s)} = \frac{2\zeta\omega_o s + \omega_o^2}{s^2 + 2\zeta\omega_o s + \omega_o^2},$$ (B.2)

where the resonant frequency of the system is $\omega_o = \sqrt{\frac{k}{m}}$, and the damping factor is $\zeta = \frac{b}{2\sqrt{km}}$. This model predicts the transfer function will have a peak at $\omega_o$, and gain slopes of 20 dB/decade and -20 dB/decade before and after the resonant frequency, respectively. Therefore noise with frequencies around $\omega_o$ might be problematic. For the isolation stage in use, $f_o \approx 2$ Hz.

The transfer function of the isolation stage can be experimentally determined by the relative motion of two sensors. Two geophones, one on the floor measuring the ground vibration, and the other on the stage measuring the transmitted motion, are used for this purpose. The time domain data were taken using a dynamic signal analyzer, and transfer function of the stage can be found by dividing their spectrums. The transfer function is shown in Figure B-3.

The data show that the stage is attenuating high frequencies, but is also amplifying lower frequencies. The resonant frequency is determined to be ~2 Hz, and the stage has positive gain for frequencies between 0.2 and 5 Hz. The experimental data follows the simulation model (Equation B.2). Therefore the stage is unable to isolate very low frequency vibrations.
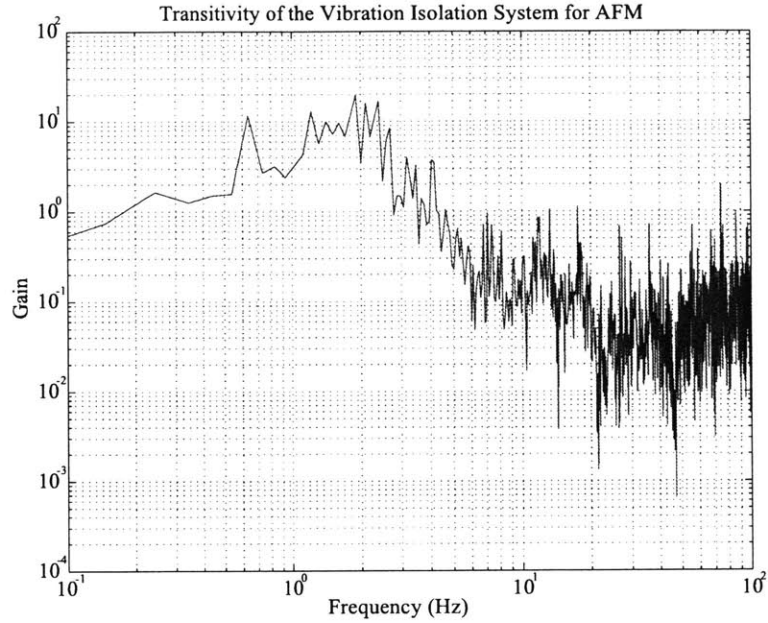
Figure B-3: Transmissibility of the vibrational isolation stage used for AFM.

## B.3   Conclusion

The total AFM noise is around ~0.118 nm, and the noise below 5 Hz is ~0.098 nm. Most of the noise is induced by ground vibrations that are amplified by the isolation stage between 0.2 and 5 Hz. To reduce the noise level, a stage with lower resonant frequency is a possible solution. With the current isolation stage, the vertical resolution is limited by this noise level.

# Appendix C

# Table of Zernike Polynomials

The Zernike polynomials are described as,

$$^{e}U_{n}^{l}(\rho, \theta) = R_{n}^{l}(\rho) \cos l\theta, \tag{C.1}$$

$$^{o}U_{n}^{l}(\rho, \theta) = R_{n}^{l}(\rho) \sin l\theta, \tag{C.2}$$

where $R_{n}^{l}$ is a radial function defined as,

$$R_{n}^{n-2m}(\rho) = \sum_{s=0}^{m} \frac{(-1)^{s}(n-s)!}{s!(m-s)!(m-n-s)!} \rho^{n-2s}, \tag{C.3}$$

The Zernike polynomials to fifth order are listed in Table C.1.

| No | n | m | l | Zernike Polynomial | Meaning |
|----|---|---|----|--------------------|---------|
| 1 | 0 | 0 | 0 | $1$ | Piston or constant |
| 2 | 1 | 0 | 1 | $\rho \sin \theta$ | Tilt about $y$-axis |
| 3 | 1 | 1 | -1 | $\rho \cos \theta$ | Tilt about $x$-axis |
| 4 | 2 | 0 | 2 | $\rho^2 \sin 2\theta$ | Astigmatism with axis $\pm 45^{o}$ |
| 5 | 2 | 1 | 0 | $2\rho^2 - 1$ | Focus shift |
| 6 | 2 | 2 | -2 | $\rho^2 \cos 2\theta$ | Astigmatism with $0^{o}$ or $90^{o}$ axis |

Table C.1: Zernike polynomials, from Malacara [20].

| No | n | m | l | Zernike Polynomial | Meaning |
|---|---|---|---|---|---|
| 7 | 3 | 0 | 3 | $\rho^3 \sin 3\theta$ | Triangular astigmatism with base on $x$-axis |
| 8 | 3 | 1 | 1 | $(3\rho^3 - 2\rho)\sin\theta$ | 3rd-order coma along $x$-axis |
| 9 | 3 | 2 | -1 | $(3\rho^3 - 2\rho)\cos\theta$ | 3rd-order coma along $y$-axis |
| 10 | 3 | 3 | -3 | $\rho^3 \cos 3\theta$ | Triangular astigmatism with base on $y$-axis |
| 11 | 4 | 0 | 4 | $\rho^4 \sin 4\theta$ | |
| 12 | 4 | 1 | 2 | $(4\rho^4 - 3\rho^2)\sin 2\theta$ | |
| 13 | 4 | 2 | 0 | $6\rho^4 - 6\rho^2 + 1$ | Spherical aberration |
| 14 | 4 | 3 | -2 | $(4\rho^4 - 3\rho^2)\cos 2\theta$ | |
| 15 | 4 | 4 | -4 | $\rho^4 \cos 4\theta$ | |
| 16 | 5 | 0 | 5 | $\rho^5 \sin 5\theta$ | |
| 17 | 5 | 1 | 3 | $(5\rho^5 - 4\rho^3)\sin 3\theta$ | |
| 18 | 5 | 2 | 1 | $(10\rho^5 - 12\rho^3 + 3\rho)\sin\theta$ | |
| 19 | 5 | 3 | -1 | $(10\rho^5 - 12\rho^3 + 3\rho)\cos\theta$ | |
| 20 | 5 | 4 | -3 | $(5\rho^5 - 4\rho^3)\cos 3\theta$ | |
| 21 | 5 | 5 | -5 | $\rho^5 \cos 5\theta$ | |

Table C.2: Zernike polynomials (continued), from Malacara [20].

# Bibliography

[1] T. C. Bailey, B. J. Choi, M. Colburn, M. Meissl, S. Shaya, J. G. Ekerdt, S. V. Sreenivasan, and C. G. Willson. Step and flast imprint lithography: Template surface treatment and defect analysis. *J. Vac. Sci. Technol. B*, 18:3572, 2000.

[2] T. C. Bailey, S. C. Johnson, S. V. Sreenivasan, J. G. Ekerdt, C. G. Wilson, and D. J. Resnick. Step and flash imprint lithography: An efficient nanoscale printing technology. *J. Photopolym. Sci. Technol.*, 15:481, 2002.

[3] J. V. Bixler, C. J. Hailey, C. W. Mauche, P. F. Teague, R. S. Thoe, S. M. Kahn, and F. B. S. Paerels. Performance of a variable line spaced master reflection grating for use in the reflection grating spectrometer on the x-ray multimirror mission. *SPIE EUV, X-ray, and Gamma-ray Istrumentation for Astronomy II*, 1549:420–428, 1991.

[4] W. A. Brantley. Calculated elastic constants for stress problems associated with semiconductor devices. *J. Appl. Phys.*, 44:534–535, 1973.

[5] C.-H. Chang, R. K. Heilmann, R. C. Fleming, J. Carter, E. Murphy, M. L. Schattenburg, T. C. Bailey, J. G. Ekerdt, R. D. Frankel, and R. Voisin. Fabrication of sawtooth diffraction gratings using nanoimprint lithography. *J. Vac. Sci. Technol. B*, 21:2755–2759, 2003.

[6] Carl Gang Chen. *Beam Alignment and Image Metrology for Scanning Beam Interference Lithography–Fabricateing Gratings with Nanometer Phase Accuracy.* PhD thesis, Massachusetts Institute of Technology, Department of Electrical Engineering and Computer Science, 2003.

[7] S. Y. Chou, P. R. Krauss, and P. J. Renstrom. Imprint of sub-25 nm vias and trenches in polymers. *Appl. Phys. Lett.*, 67:3114, 1995.

[8] D. R. Ciarlo. Corner compensation structures for (11) oriented silicon. *Proceedings of the IEEE Micro Robots and Teleoperators Workshop, Hyannis, MA*, pages 6/1–4, 1987.

[9] M. Elwenspoek. On the mechanism of anisotropic etching of silicon. *J. Electrochem. Soc.*, 140:2075–2080, 1993.

[10] Juan Ferrera. *Nanometer-Scale Placement in Electron-Beam Lithography*. PhD thesis, Massachusetts Institute of Technology, Department of Electrical Engineering and Computer Science, 2000.

[11] C. R. Forest, C. R. Canizares, D. R. Neal, M. McGuirk, A. H. Slocum, and M. L. Schattenburg. Metrology of thin transparent optics using shack-hartmann wavefront sensing. *Opt. Eng.*, 43:742, 2004.

[12] A. E. Franke, M. L. Schattenburg, E. M. Gullikson, J. Cottam, S. M. Kahn, and A. Rasmussen. Super-smooth x-ray reflection grating fabrication. *J. Vac. Sci. Technol. B*, 15:2940–2945, 1997.

[13] Andrea Elke Franke. *Fabrication of Extremely Smooth Nanostructures Using Anisotropic Etching*. M.S. thesis, Massachusetts Institute of Technology, Department of Electrical Engineering and Computer Science, 1997.

[14] L. B. Freund and S Suresh. *Thin Film Materials: Stress, Defect Formation and Surface Evolution*. Cambridge University Press, 2003.

[15] Leonid I Goray. Rigorous efficiency calculations for blazed gratings working in in- and off-plane mountings in the 5-50-a wavelengths range. *Proc. SPIE*, 5168:260, 2004.

[16] D. L. Kendall. On etching very narrow grooves in silicon. *Appl. Phys. Lett.*, 26:195–198, 1975.

[17] D. L. Kendall. Vertical etching of silicon at very high aspect ratios. *Ann. Rev. Mater. Sci.*, 9:373–403, 1979.

[18] Paul Thomas Konkola. *Design and Analysis of a Scanning Beam Interference Lithography System for Patterning Gratings with Nanometer-level Distortions.* PhD thesis, Massachusetts Institute of Technology, Department of Mechanical Engineering, 2003.

[19] Marc Madou. *Fundamentals of Microfabrication.* CRC Press, 1997.

[20] Daniel Malacara. *Optical Shop Testing.* John Wiley & Sons, Inc, 1992.

[21] T. M. Mayer, M. P. de Boer, N. D. Shinn, P. J. Clews, and T. A. Michalske. Chemical vapor deposition of fluoroalkylsilane monolayer films for adhesion control in microelectromechanical systems. *J. Vac. Sci. Technol. B*, 18:2433, 2000.

[22] A. G. Michette and C. J. Buckley. *X-ray Science and Technology.* Institute of Physics Publishing, 1993.

[23] O. Mongrard. *High Accuracy Foil Optics for X-ray Astronomy.* M.S. thesis, Massachusetts Institute of Technology, Department of Aeronautics and Astronautics, 2001.

[24] Christopher Palmer. *Diffraction Grating Handbook.* Thermo RGL, 2002.

[25] A. Rasmussen, A. Aquila, J. Bookbinder, C.-H. Chang, E. Gullikson, R. K. Heilmann, S. M. Kahn, F. Paerels, and M. L. Schattenburg. Grating arrays for high-throughput soft x-ray spectrometers. *Proc. SPIE*, 5168:248, 2004.

[26] M. L. Schattenburg, R. J. Aucoin, and R. C. Fleming. Optically matched trilevel resist process for nanostructure fabrication. *J. Vac. Sci. Technol. B*, 13:3007–3011, 1995.

[27] H. Seidel, L. Csepregi, A. Heuberger, and H. Baumgartel. Anisotropic etching of crystalline silicon in alkaline solutions-part i. orientation dependence and behavior of passivation layers. *J. Electrochem. Soc.*, 137:3612–3626, 1990.

[28] Stephen D. Senturia. *Microsystem Design*. Kluwer Academic Publishers, 2001.

[29] J. Strong. The john's hopkin university and diffraction grating. *J. Opt. Soc. Am*, 50:1148–1152, 1960.

[30] WaveFront Sciences, Inc., 14810 Central Ave SE, Albuquerque, NM 87123. *Complete Light Analysis System–2D User's Manual*, 2002.